FINAL TECHNICAL REPORT

U.S. Department of Energy National Energy Technology Laboratory

Co-operative Agreement: DE-FE0023314

Project Title: Development of Geomechanical Screening Tools to Identify Risk: An Experimental and Modeling Approach for Secure CO_2 Storage

Principal Investigator: Dr. Mary F. Wheeler (Director)
512-475-8626
mfw@ices.utexas.edu

Submission Date: December 26, 2017

DUNS Number: 170230239

The University of Texas at Austin
P. O. BOX 7726

Austin, Texas 78713-7726

Project Period: September 1, 2014 – August 31, 2017

Report Frequency: Final Technical Report

Signature: 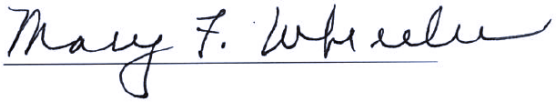

DISCLAIMER

This report was prepared as an account of work sponsored by an agency of the United States Government. Neither the United States Government nor any agency thereof, nor any of their employees, makes any warranty, express or implied, or assumes any legal liability or responsibility for the accuracy, completeness, or usefulness of any information, apparatus, product, or process disclosed, or represents that its use would not infringe privately owned rights. Reference herein to any specific commercial product, process, or service by trade name, trademark, manufacturer, or otherwise does not necessarily constitute or imply its endorsement, recommendation, or favoring by the United States Government or any agency thereof. The views and opinions of authors expressed herein do not necessarily state or reflect those of the United States Government or any agency thereof.

ABSTRACT

CO_2 injection in the subsurface introduces additional complexity in terms of interactions of the reservoir host pore fluid with natural heterogeneity of hydro-mechanical properties of the rock. Natural heterogeneity of the reservoir rock and caprock formations includes spatial variation of hydro-mechanical properties as well as the presence of natural fractures. We developed a coupled mathematical modeling and experimental framework that takes into account the effect of rock heterogeneity on effective mechanical properties of the rock in contact with CO_2. We performed accurate laboratory experimetns to determine the changes in rock mechanical properties due to mineral dissolution in the presence of carbonic acid generated by CO_2 injection. A two-scale adaptive homogenization framework was then developed to consistently upscale petrophysical and geomechanical properties to the field scale. Further, we also developed high-fidelity, numerical solution schemes, non-linear and linear solvers and preconditioners to solve the coupled flow, reactive transport and geomechanical system. The numerical model was then used to study field scale CO_2 sequestration problems for the two selected field sites: (1) Frio formation and (2) Cranfield site. We also developed robust schemes for field data assimilation, model calibration such that the residual uncertainty at the end of the data assimilation procedures can be faithfully represented while taking into account the coupled geochemical and geomechanical processes.

TABLE OF CONTENTS

EXECUTIVE SUMMARY

In-depth understanding of the long-term fate of CO_2 in the subsurface requires study and analysis of the reservoir formation, the overlaying caprock formation, and adjacent faults. Caprock flaws, such as pre-existent and induced fractures constitute the most likely paths for CO_2 leakage. Natural fractures can be re-activated (shear fractures) or re-opened (open-mode fractures) by increases in pore pressure during injection. Increases in pore pressure of a few MPa are non-negligible and can constitute a serious threat to safe CO_2 storage. The proposal is to study these issues using a combination of carefully conceived laboratory experiments, upscaling schemes for bridging between the experimental and field scales, accurate numerical models to model couple chemo-thermo-mechanical processes associated with long term storage of CO_2 in the subsurface and finally implementing robust validation schemes using field data from the Frio and Cranfield sites. The specific key project objectives are to (1) measure petrophysical and hydro-mechanical properties of rocks in the presence of CO_2 in the laboratory, (2) develop upscaling methods for rock petrophysical and hydro-mechanical properties considering natural heterogeneity and pre-existing fractures, (3) develop advanced and cost-effective coupled solvers for CO_2 injection flow simulation and geomechanics, (4) simulate numerically and perform history matching using CO_2 injection at Frio and Cranfield sites, (5) implement schemes for quantifying the residual uncertainty after model calibration and data assimilation, (6) develop guidelines and workflow to mitigate the geomechanical risks of CO_2 injection in the subsurface.

The research team has developed a framework for risk assessment and performance evaluation of different CO2 sequestration scenarios. This framework includes combined laboratory experiments, numerical modeling of the coupled processes, and uncertainty and parameter estimation for selected field sites as listed below:

- Measurement of petrophysical properties of Cranfield rocks from field cores and well logs. Laboratory testing of Cranfield rocks for changes in mechanical properties with CO_2 specific loading.
- Mathematical and numerical modeling of coupled multiphase flow, transport, and geomechanical processes. A hysteretic relative permeability and capillary pressure model was developed and implemented in IPARS that accurately describes a dominant mechanism of CO_2 trapping in subsurface aquifers.
- A general upscaling framework using adaptive numerical homogenization for non-linear, multiphase flow and transport. This technique was verified using a standalone implementation and benchmarked for computational efficiency and solution accuracy.

- Development of a multiple-realization optimizer coupled with IPARS, parameter estimation using ensemble filtering approach, and uncertainty quantification using an adaptive response surface-based technique.

A detailed description of all the tasks/activities performed as stipulated in the project milestones can be found in the corresponding quarterly report. This final report summarizes the major tasks and accomplishments performed under this award.

Task 2.0 – Laboratory Experiments for Petrophysical and Hydro-mechanical Rock Properties

Subsurface CO2 injection and storage alters formation pressure. Changes of pore pressure may result in fault reactivation and hydraulic fracturing if the pressure exceeds the corresponding thresholds. Most simulation models predict such thresholds utilizing relatively homogeneous reservoir rock models and do not account for CO_2 dissolution in the brine phase to calculate pore pressure evolution. This study presents an estimation of reservoir capacity in terms of allowable injection volume and rate utilizing the Frio CO_2 injection site in the coast of the Gulf of Mexico as a case study.

The work includes laboratory core testing, well-logging data analyses, and reservoir numerical simulation. We built a fine-scale reservoir model of the Frio pilot test in our in-house reservoir simulator IPARS (Integrated Parallel Accurate Reservoir Simulator). We first performed history matching of the pressure transient data of the Frio pilot test, and then used this history-matched reservoir model to investigate the effect of the CO_2 dissolution into brine and predict the implications of larger CO_2 injection volumes. Our simulation results –including CO_2 dissolution– exhibited 33% lower pressure build-up relative to the simulation excluding dissolution.

Capillary heterogeneity helps spread the CO_2 plume and facilitate early breakthrough. Formation expansivity helps alleviate pore pressure build-up. Simulation results suggest that the injection schedule adopted during the actual pilot test very likely did not affect the mechanical integrity of the storage complex. Fault reactivation requires injection volumes of at least ~ sixty times the actual injected volume at the same injection rate. Hydraulic fracturing necessitates much larger injection rates than the ones used in the Frio pilot test. Tested rock samples exhibit ductile deformation at in-situ effective stresses. Hence, we do not expect an increase of fault permeability in the Frio sand even in the presence of fault reactivation.

The purpose of this study is to investigate pore pressure build-up induced by CO_2 injection in heterogeneous and compartmentalized poorly consolidated sands. We utilize the Frio CO_2 project as a case study. The paper starts with a description of the reservoir model, petrophysical and geomechanical properties (based on laboratory experiments and well-logging analyses), and the compositional phase behavior model. Then, we show the results of history matching for the actual injection schedule and extend conclusions for larger injection volumes and rates. We conclude with an evaluation of expected geomechanical perturbations and limits for injection volumes and rates based on the current in-situ state of stress and compartmentalization assumption.

Reservoir Geometry, Boundary Conditions and Simulation Grid

The detailed area of study (DAS) is a subdomain of interest in the larger Frio reservoir which includes injection and observation wells. The DAS boundaries are determined by faults and a salt dome North-West of the reservoir (Figure 2.1-a). The reservoir dips 16° towards the South-East. We adopted no-flow boundary conditions for all four boundaries. The lower end of the reservoir is an idealized as an elongated section up to 12 km long (Figure 2.1-b). Fault 2 and 3 are represented by low permeability planes embedded in the middle of the DAS area. All four faults are normal faults having same strike about N45°W but with different dip angles as interpreted from seismic images and earlier developed models (Hovorka et al., 2006) (Table 2.1).

The total thickness of the model is 30 m (100 ft) evenly divided into 50 grid blocks of 0.6 m (2 ft)

perpendicular to bedding in the x-direction. Parallel to the bedding pane, the model is divided into 78 grid blocks in the y-direction (853 m) and 71 grid blocks in the z-direction (12192 m). The injection zone (approximately 49 m by 61 m (160 ft by 200 ft)) is refined parallel to the bedding (y and z-directions) with 1.5 m (5 ft) grid blocks, and the surrounding area is spaced with gradually larger sizes of the blocks from 3 m (10 ft) to 305 m (1,000 ft). The full DAS model has 276,900 degrees of freedom. The well injection schedules replicated the field injection/shut-in schedule. Further the initial reservoir pressure was populated using full observation of base pressure at the injection and observation wells.

Frio C sand is composed of subarkosic fine-grained, moderately sorted quartz and feldspar sand grains; with minor amounts of illite, smectite, and calcite (Kharaka et al. 2006). These minor amounts of clay and calcite are located at grain contacts and may affect dynamic elastic properties (Al Hosni et al., 2016). We obtained petrophysical properties from laboratory tests courtesy of GCCC (Gulf Coast Carbon Center, UT Austin) and petrophysical and geomechanical properties from experiments performed in our laboratory. Table 2.2 summarizes specimen depths and experiments performed.

Porosity and Permeability

Experimental measurements as well as well-logging analysis (data courtesy of the GCCC) provided petrophysical properties and geomechanical properties for populating the reservoir model. The well-logging analysis is used to calculate porosity and permeability, respectively from data spaced every 0.15 m (0.5 ft). We corrected measured neutron porosity ϕ_N and density porosity ϕ_D for the presence of clays according to Equations (1-2) (Torres-Verdin, 2016).

$$\phi_{\mathrm{D}}^{c} = \frac{\phi_D - C_{sh}\phi_{D,sh}}{1 - C_{sh}} \tag{1}$$

$$\phi_{\mathrm{N}}^{c} = \frac{\phi_N - C_{sh}\phi_{N,sh}}{1 - C_{sh}} \tag{2}$$

where ϕ_{D}^{c} and ϕ_{N}^{c} are shale-corrected density porosity and neutron porosity, C_{sh} is volumetric concentration of shale, and $\phi_{D,sh}$ and $\phi_{N,sh}$ are apparent density porosity and neutron porosity of pure shale. The selected depths for the shale correction are 1516 m (4972.5 ft) for the clay-rich layer (local maximum GR) and 1544 m (5065.5 ft) for the water saturated clay-poor layer (local minimum GR). Table 2.3 shows the well log GR readings at the two depths. The corrected porosity ϕ_{S}^{c} is

$$\phi_{\mathrm{S}}^{c} = \sqrt{\frac{\left(\phi_D^c\right)^2 + \left(\phi_N^c\right)^2}{2}} \tag{3}$$

We calculated permeability along the entire injection zone using an empirical correlation between laboratory measured porosity ϕ and permeability k (Figure 2.2). Figure 2.3 shows the resulting corrected porosity and permeability including layers above and below the injection zone. Reservoir properties were averaged from the calculated data; namely, the grid block spatial scale of 0.6 m (2 ft) see Figures 2.3-a and b for interpolated values of porosity and permeability. We adjusted the ratio between vertical and horizontal permeabilities to 1/3 in order to achieve history matching in the pressure response.

Capillary Pressure and Relative Permeability

Capillary pressure measurements suggest that the layered formation can be categorized into different

groups of rock depending on the values of the J-function:

$$J(S_w) = \frac{P_c(S_w)}{\gamma cos\theta}\sqrt{\frac{k}{\phi}} \quad (4)$$

where Sw is saturation of water, Pc is capillary pressure, γ is interfacial tension, and θ is contact angle (Peters, 2012). We used the J-functions to classify the full reservoir model into four different rock types to build an accurate reservoir model (Table 2.4). Figure 2.4-b shows the capillary pressure, and a mapping using converted J-functions from an air-mercury system with interfacial tension at 485 mN/m and contact angle 140° to CO2-brine system with interfacial tension 30 mN/m and contact angle 40° (Espinoza and Santamarina, 2010). We employed a Brooks-Corey drainage model to calculate the relative permeability curves from capillary pressure data (Figure 2.4-b and -c).

$$P_c = P_e(S_w^*)^{-\frac{1}{\lambda}} \quad (5)$$

$$S_w^* = \frac{S_w - S_{wirr}}{1 - S_{wirr}} \quad (6)$$

where Pe is the capillary entry pressure, S_w^* is the reduced wetting phase saturation, λ is the pore size distribution index, and Swirr is irreducible water saturation. The corresponding relative permeabilities are

$$k_{rw}(S_w) = (S_w^*)^{\frac{2+3\lambda}{\lambda}} \quad (7)$$

$$k_{rnw}(S_w) = k_{nwr}\left(1 - \frac{S_w - S_{wirr}}{S_m - S_{wirr}}\right)^2\left[1 - (S_w^*)^{\frac{2+\lambda}{\lambda}}\right] \quad (8)$$

where krw is the relative permeability of wetting phase (brine), krnw is the relative permeability of non-wetting phase (CO2), Sm (= 1 for drainage) is the wetting phase saturation corresponding to the critical non-wetting phase saturation, and knwr is the non-wetting phase relative permeability at the irreducible wetting phase saturation. Table 2.4 lists the modelling parameters used to calculate the relative permeability curves (Figure 2.4-c). The reservoir model assimilates heterogeneity of capillary pressure and relative permeability as shown in Figure 2.4-c.

Geomechanical Properties

We quantified Frio sand rock compressibility using step loading of pore pressure and confining stress (Bouteca et al., 1999) (Figure 2.5-a). We saturated sample V1 with synthetic 93,000 ppm salinity NaCl solution as pore fluid and measured volumetric as a function of effective mean stress (Figure 2.5-b) . The corresponding bulk rock compressibility is 4.6 ·10-8 MPa-1 (6.3 ·10-6 psi-1) evaluated using the following equations assuming negligible mineral compressibility

$$C_p = \frac{1}{V_p}\frac{\Delta V_p}{\Delta P_p} = \frac{\Delta \varepsilon_{vol}}{\Delta P_p} \quad (9)$$

Calculated rock compressibility was taken to be constant throughout the reservoir.

We also conducted a multistage deviatoric loading test to evaluate strength and post-peak failure behavior of the Frio C sand. The multistage loading consisted of increasing deviatoric stress at three different constant confining stresses: 3.4 MPa (500 psi), 6.9 MPa (1,000 psi), and 10.3 MPa (1,500 psi) (Figure

2.6-a). During the first two loading stages, the sample exhibited dilative behavior by increasing deviatoric stress. Finally, shear yield was allowed at the last loading stage. The sand resulting friction

angle is about 38º, and the cohesive strength is zero (Figure 2.6-b). The sand undergoes ductile deformation at peak stress.

In-situ Stresses

We estimated the magnitude and direction of principal stresses using an overburden (total vertical stress) gradient of 20.5 MPa/km (0.907 psi/ft) (Hovorka et al., 2003) that includes the effect of the rising salt dome on "dome hoop stresses" (minimum principal stress oriented in circumferential direction - Nikolinakou et al., 2014). We assumed a limit frictional equilibrium of the sand unit (Zoback, 2007) (friction angle from Section 2.2) and a normal faulting regime from the seismic interpretation of strikes and dips of the respective faults (Figure 2.1). The vertical-to-horizontal stress anisotropy is

$$\frac{\sigma_1}{\sigma_3} = \frac{S_v - P_p}{S_{hmin} - P_p} \leq \frac{1+sin\,(\varphi)}{1-sin\,(\varphi)} \qquad (10)$$

where σ1 and σ3 are maximum and minimum principal effective stress φ is the friction angle, Sv is the total vertical stress, Shmin is the minimum total horizontal stress, and Pp is the pore pressure. At the perforation depth of the injection well, measured bottomhole pressure Pp was 14.8 MPa (2153 psi), and calculated Sv was 31.6 MPa (4580.4 psi). Using φ = 38° (Figure 2.6), limit frictional equilibrium provides an estimate of the lower bound of minimum principal stress (horizontal) around the injection zone. This value was estimated to be 18.8 MPa (2,734 psi).

Stress anisotropy may decrease with time due to creep. Hovorka et al. (2003) calculated formation fracture pressure equal to 26.6 MPa (3,851 psi) at a depth of 1,667 m (5,000 ft) based on Eaton's equation using Poisson's ratio ν = 0.416, overburden gradient 0.907 psi/ft, and reservoir pressure gradient 0.432 psi/ft.

$$S_{hmin} = \left(\frac{\nu}{1-\nu}\right)(S_v - P_p) + P_p \qquad (11).$$

History Match

Figure 2.7 shows history-matching of pressure responses for four injection cycles in the base case, including injection and shut-in periods for both the injection and observation wells. The pressure response in the first injection cycle does not coincide with simulation results. This peak might have occurred due to effects of formation damage or near-wellbore perforation complexity. However, the CO_2 breakthrough time was predicted by numerical simulation to the 2.3 days as compared to 2.1 days observed in field.

Figure 2.8 shows snapshots of the CO_2 plume migration up to 60 days after injection. The CO_2 plume moves toward the observation well due to buoyancy but does not move above the few permeability caprock. Figure 2.8-a shows the total CO_2 concentration (CO_2 [lb-mole]/pore volume [ft^3]) in both gas phase and dissolved phase while Figure 2.8-b shows CO_2 saturation of the gas phase only (bulk supercritical CO_2). Initially, the two figures show similar CO_2 saturation distribution since the CO_2 has not dissolved extensively into brine yet. After 30 days of the injection, the difference between Figures 2.8-a and -b demonstrates a considerable amount of dissolved CO_2 around injection zone (approximately

30%).

Rock compressibility C_p is one of the key mechanical properties determining pore pressure buil-up. Rock compressibility lowers the pore pressure buildup at the injection well by increasing available pore volume. Zero rock compressibility results in a steady increase of wellbore pressure for rate specified injection well. In fact the pressure buildup is twice for zero rock compressibility compared to the field observations at both injection and observation wells. We therefore assume a non-zero rock compressibility estimated from the laboratory experiment in our numerical simulation model; as described before. The simulation results show flattening pressure transient curve during constant injection rate.

Injection Rate to Induce Fault Activation

This section applied results of reservoir simulation to determine critical pore pressures and injection rates for fault reactivation. Normal and shear stresses are calculated at four faults from the estimated principal stresses in Section 2.2.4. The stress tensor in geographical coordinates is obtained by applying a transformation matrix R_1 to the principal stress tensor as shown below:

$$S_g = R_1^T S R_1 = R_1^T \begin{bmatrix} S_1 & 0 & 0 \\ 0 & S_2 & 0 \\ 0 & 0 & S_3 \end{bmatrix} R_1 \quad (15),$$

where

$$R_1 = \begin{bmatrix} cos\,a\,cos\,b & sin\,a\,cos\,b & -sin\,b \\ cos\,a\,sin\,b\,sin\,c - sin\,a\,cos\,c & sin\,a\,sin\,b\,sin\,c + cos\,a\,cos\,c & cos\,b\,sin\,c \\ cos\,a\,sin\,b\,cos\,c + sin\,a\,sin\,c & sin\,a\,sin\,b\,cos\,c - cos\,a\,sin\,c & cos\,b\,cos\,c \end{bmatrix} \quad (16),$$

and Euler rotation angles a = 44.85°, b 90°, and c = 0° for the location shown in Figure 2.1 (Zoback, 2007).

For stress analysis, the stress tensor in the geographical coordinate system S_g is projected onto the fault plane coordinate system using observed fault strikes and dip angles (Table 2.1). Transformation vectors n_n and n_d, (function of fault strike *str* and dip *dip*) permit calculating the magnitudes of shear stress τ and normal stress S_n on the fault plane from the stress tensor in geographical coordinate system S_g.

$$\tau = \{S_g[n_n]\}^T n_d = \left\{ S_g \begin{bmatrix} -\sin(str)\sin(dip) \\ \cos(str)\sin(dip) \\ -\cos(dip) \end{bmatrix} \right\}^T \begin{bmatrix} -\sin(str)\cos(dip) \\ \cos(str)\cos(dip) \\ sin(dip) \end{bmatrix} \quad (17),$$

$$S_n = \{S_g[n_n]\}^T n_n = \left\{ S_g \begin{bmatrix} -\sin(str)\sin(dip) \\ \cos(str)\sin(dip) \\ -\cos(dip) \end{bmatrix} \right\}^T \begin{bmatrix} -\sin(str)\sin(dip) \\ \cos(str)\sin\,(dip) \\ -\cos\,(dip) \end{bmatrix} \quad (18),$$

Figure 2.9 shows the stress conditions at each fault at initial pore pressure condition before the injection assuming a non-zero cohesive strength in the rock matrix. The values of principal stresses change depending on the depth. The value of principal stresses at the injection well is specified in Section 2.2.4. As pore pressure increases, the effective normal stress on the fault plane decreases and the Mohr circle

moves towards the yield line increasing the possibility of the shear yield at the fault plane.

Figure 2.10 shows the maximum amount of CO_2 injection without causing fault reactivation as a function of injection rate. The maximum cumulative amount of CO_2 injection is about 130,000 tons, and it is relatively dependent of injection rates. The first location of fault reactivation (Fault 2) is observed for all injection rate cases (Table 2.7). Extremely high injection rates over 10,000 tons/day may fracture the well before causing fault reactivation.

Overall, the results indicate that the first Frio pilot test injected less than 1.6% of the minimum possible amount of CO_2 storage without perturbing faults (Figure 2.10). Assumption of negligible rock compressibility results a reduction of storage capacity by a factor of ten. These values are provided as an illustrative comparison for compartmentalized reservoirs in formations near the limit of stress equilibrium. Actual predictions need to measure in-situ stress magnitude and orientation and should account for flow boundary conditions that may allow for leaks at faults.

Tertiary unconsolidated sands and mudrocks at Frio do not exhibit brittle deformation during shearing. Figure 2.6-a shows slight strain hardening behavior of Frio sand at in-situ effective stresses. Large induced seismicity events and failure localization (and local increases in permeability) are less likely to occur in geological formations that sustain large plastic strains at yield.

Injection Rate to Induce Open-Mode Fractures

Figure 2.10 summarizes simulation results showing the maximum amounts of CO_2 injection needed to fracture the injection well (assuming that bottom hole pressure reaches the minimum principal stress) and zero fault leakage upon reactivation. If faults are leaky, then an open-mode fracture may not develop due to the pore pressure control at faults. Fault reactivation predates hydraulic fracturing for typical injection rates < 10,000 ton per day. Injection rates above 10,000 tons per day can cause hydraulic fracturing before fault reactivation and are not affected by domain size because of the sharp pressure gradient developed around the injection wellbore (Table 2.7). Hovorka et al. (2003) suggested a maximum injection rate of 250 tons per day. Injection pressure and rate used at the first Frio pilot test seems to be significantly below thresholds for developing open-mode fractures.

Pore Pressure Reduction Due to CO_2 Dissolution into Brine

Immiscible two-phase fluid flow simulation (Simulation IM) shows 75.9 kPa (11 psi) higher pressure response compared to compositional Simulation BC due to no dissolution of CO_2 into the brine (Figure 2.7). The amount of dissolved CO_2 in Simulation BC increases with time as the plume spreads in the brine-saturated reservoir. The binary interaction coefficient, one of the key parameters of CO_2 solubility in brine, has large effects on the pore pressure for a given injection scenario. At the end of injection, approximately 20% of the CO_2 was dissloved in the brine. After 20 days of the end of injection, 44% of the injected CO_2 was dissolved into the brine, and eventually, 91% of the CO_2 was dissolved after 95 days (Figure 2.8). The CO_2 plume in immiscible simulation (IM) is thinner and moves faster than that in simulation using BC. Results indicate that CO_2 dissolution contributes a fair proportion to trapping for small CO_2 injection volumes. CO_2 dissolution in the brine phase alleviates pore pressure buildup and extends injection times without effecting mechanical stability compared to the immiscible case. We predict that injection can be carried out for an additional two days at 200 tons per day. The effect of

dissolution on pore pressure buildup is stronger in rocks with low pore compressibility.

Figures

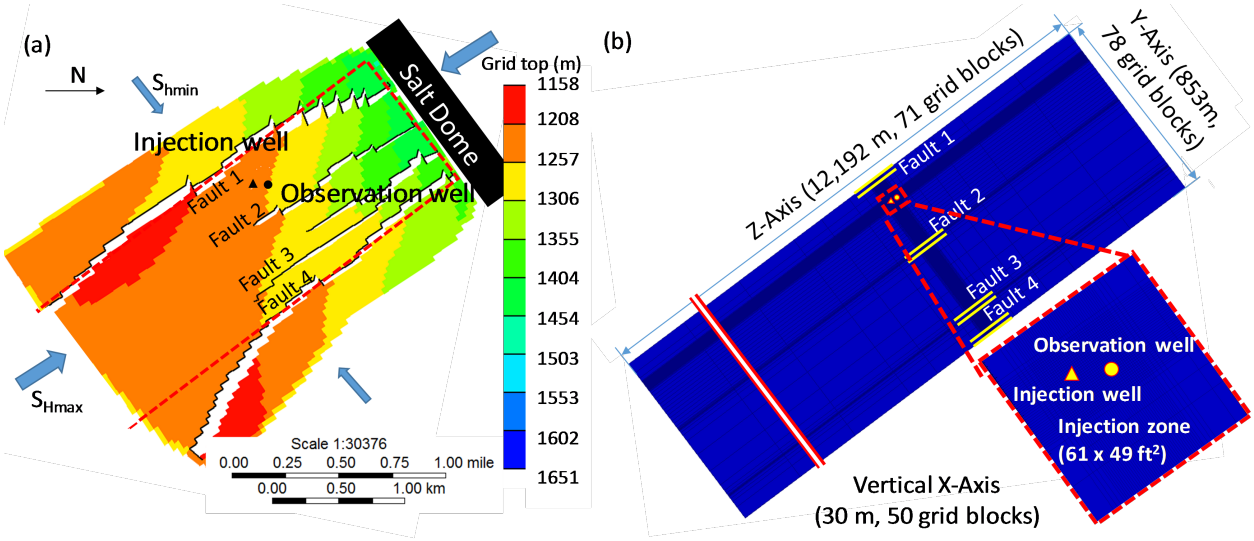

Figure 2.1. (a) Schematic diagram of Frio structure (Top view). The dashed red box is the selected region for building a DAS reservoir. (b) Detailed area of study reservoir model geometry and zoom-in into the grid refinement around the injection zone. Double-yellow lines show the faults locations analyzed in this study.

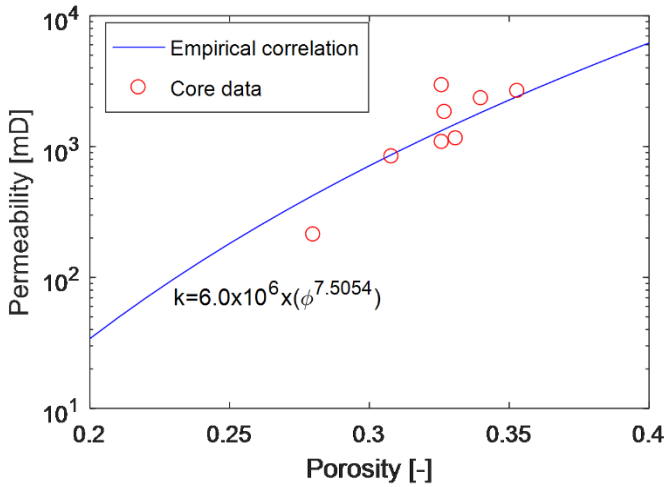

Figure 2.2. Porosity and permeability empirical relationship from core measurements.

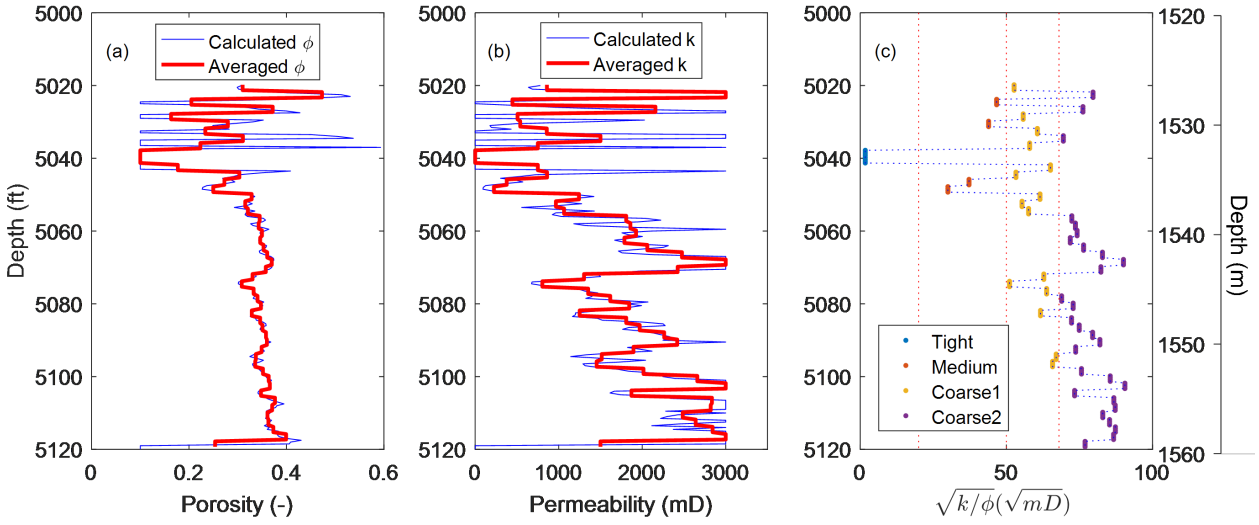

Figure 2.3. (a) Porosity, (b) permeability, and (c) ratio $\sqrt{k/\phi}$ around the injection well as a function of measured depth: calculated from well-logs (blue line), adopted in model (red line).

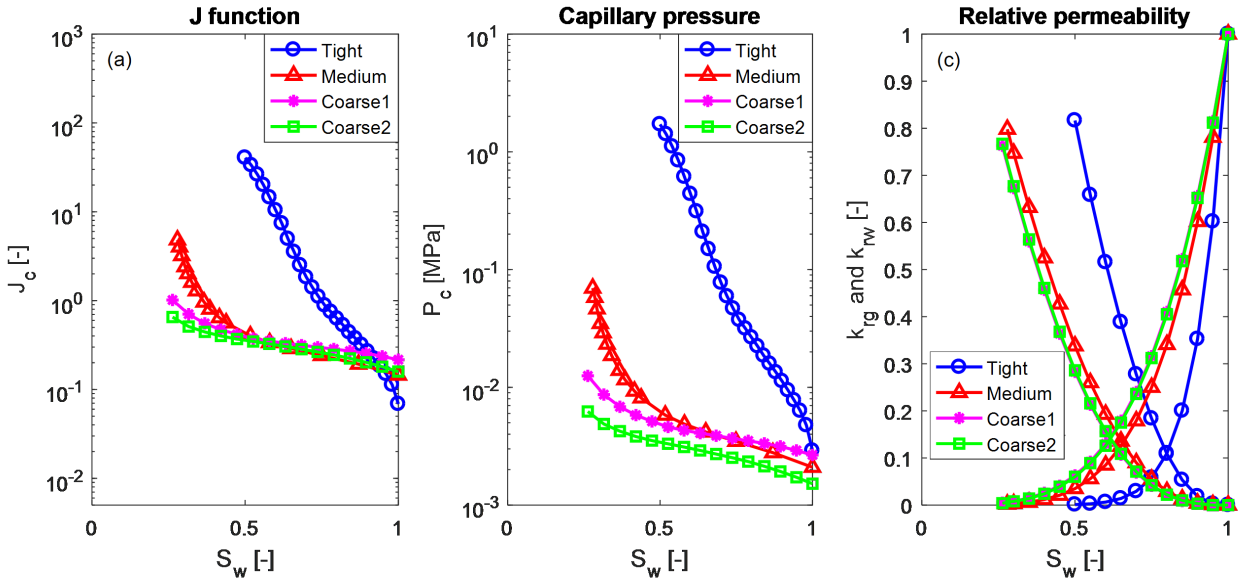

Figure 2.4. (a) J-function, (b) capillary pressure, and (c) relative permeability of four rock types assimilated into the reservoir model.

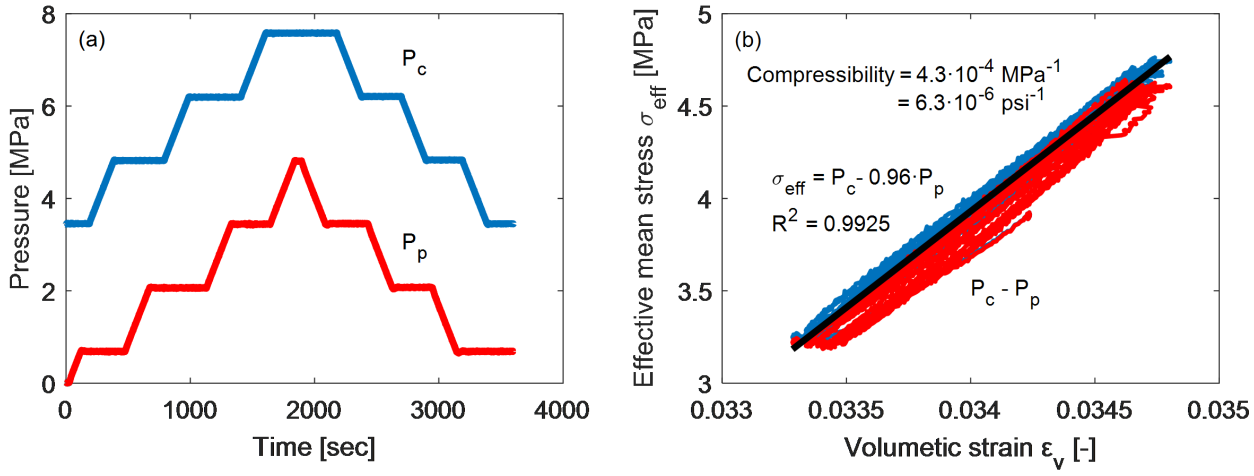

Figure 2.5. Results of pore pressure and confining stress loading and unloading on Frio sand: (a) loading paths of pore pressure P_p and confining stress P_c (b) volumetric stress change as a function of effective mean stress. The resulting Biot coefficient is 0.96.

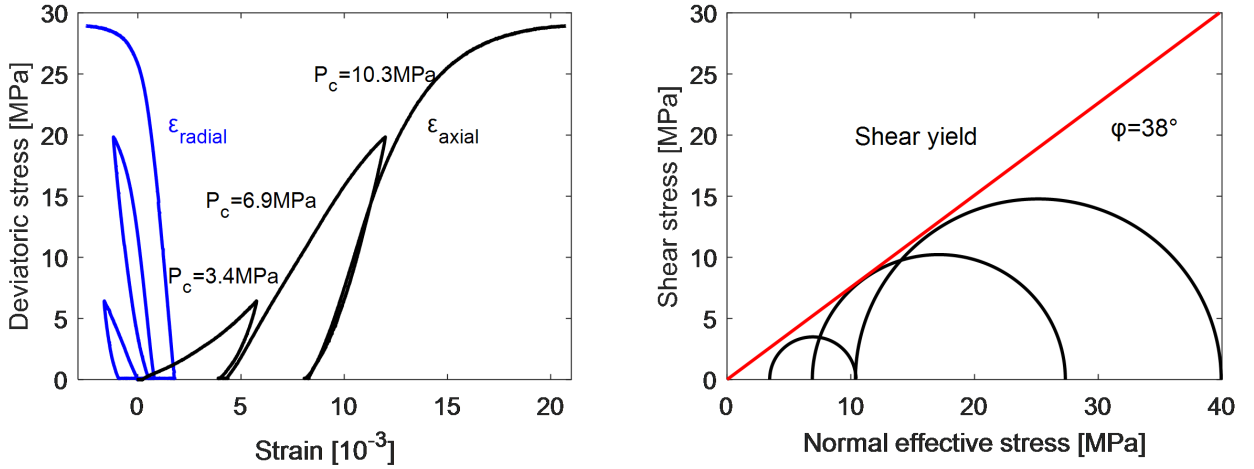

Figure 2.6. Results of multistage triaxial loading on Frio sand at confining stress 3.4 MPa, 6.9 MPa and 10.3 MPa: (a) deviatoric stress as a function of axial and radial strains and (b) Mohr-Coulomb shear yield line.

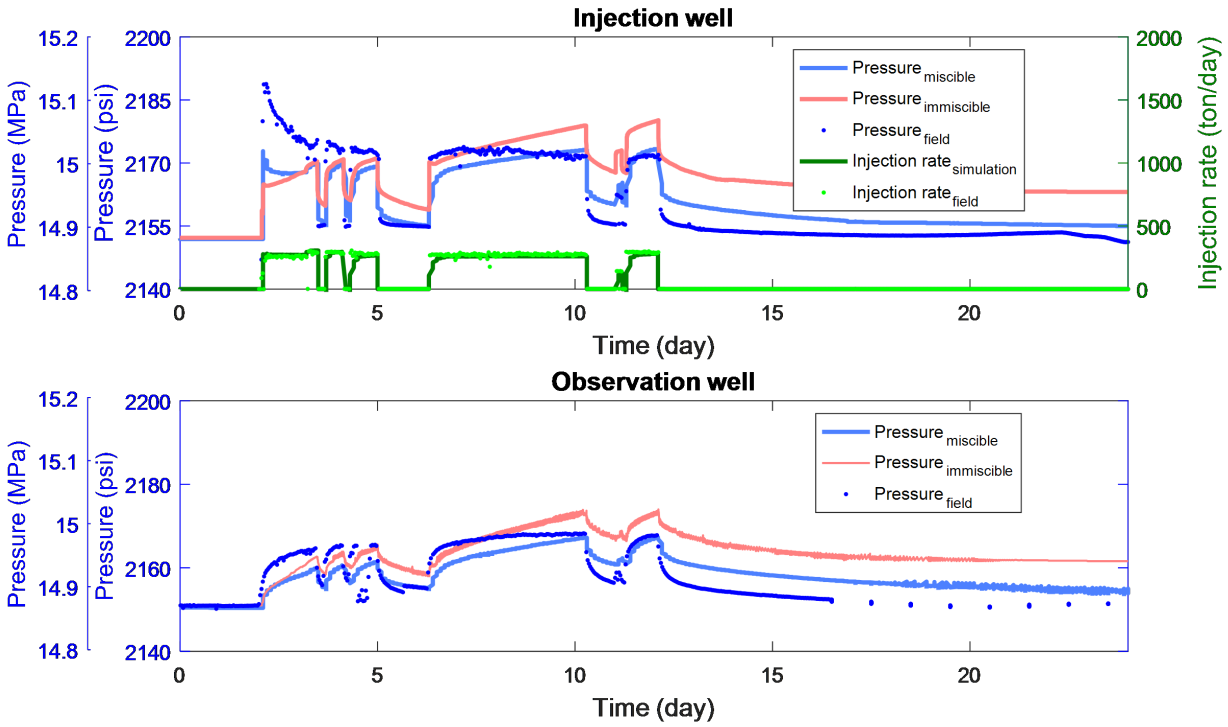

Figure 2.7. Injection rate and the bottom-hole pressure response at the injection well of Frio field and history matched simulation results.

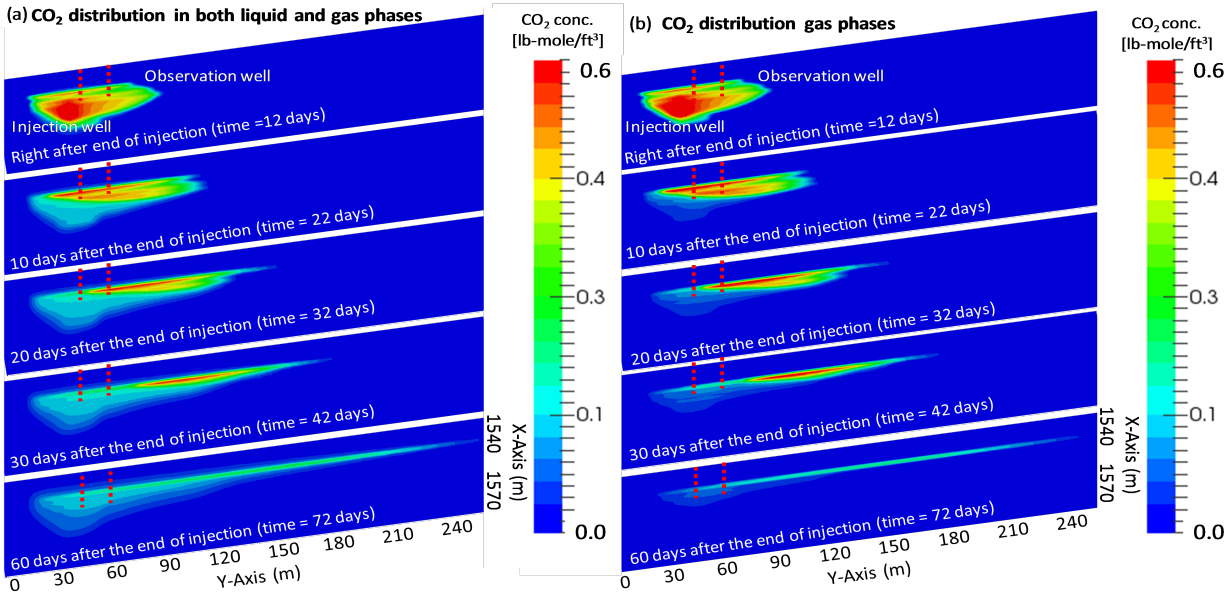

Figure 2.8. History-matched simulation: (a) CO_2 concentration in both gas phase and dissolved phase and (b) CO_2 concentration in gas phase along a cross section passing by the injection and observation wells (1 lb-mole/ft^3 = 16.0 mole/L).

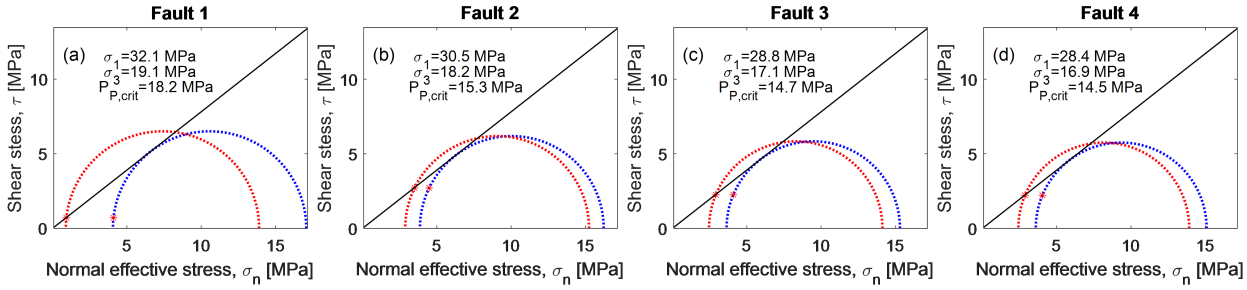

Figure 2.9. Effective stress Mohr circles at initial pore pressure (blue) and critical pore pressure (red). Red star shows the state of stress at Fault 1 (a), Fault 2 (b), and Fault 3 (c). In-situ stresses are assumed based on stress limit equilibrium. Results illustrate the effect of pore pressure increase at faults.

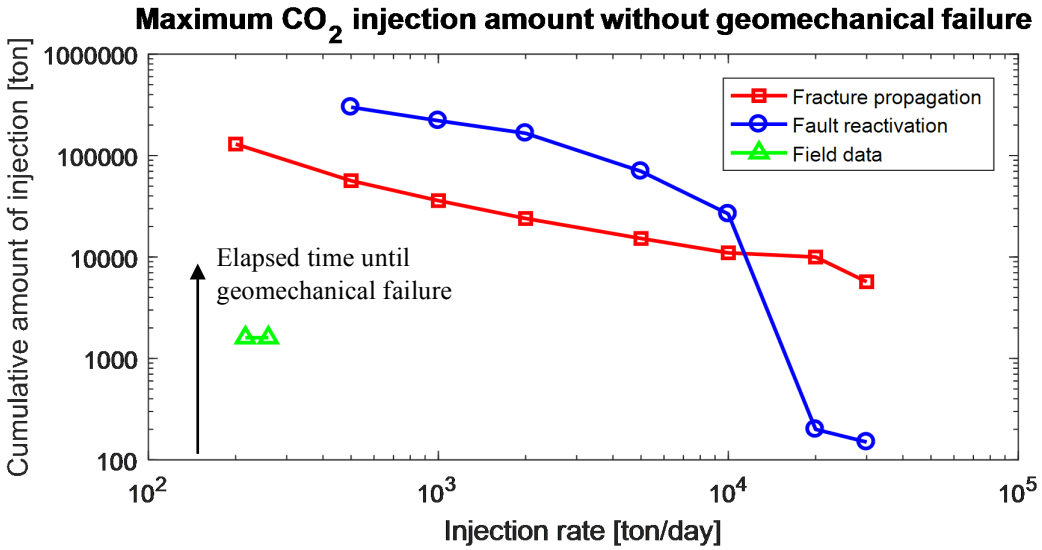

Figure 2.10. The cumulative amount of CO_2 injection without causing fault reactivation (solid blue line) or hydraulic fracture at the injector (solid red line) as a function of injection rate assuming closed reservoir compartments. Green triangles show actual cumulative CO_2 injection volume and injection rates attained in the field during the first Frio pilot test.

Table 2.1. Information about faults in DAS

	Depth (closest to injection well)	Strike	Dip
Fault 1	1,566 m (5,139 ft)	N45°W	87°NE
Fault 2	1,542 m (5,060 ft)	N45°W	77°NE
Fault 3	1,458 m (4,873 ft)	N45°W	77°NE
Fault 4	1,408 m (4,621 ft)	N45°W	78°NE

Table 2.2. Information of samples from laboratory experiments

Depth [ft]	Depth [m]	Plug direction	Type of experiments	Porosity [-]	Permeability [mD]
5051.8	1539.8	Horizontal	Gas permeability, MICP (GCCC)	0.308	837
5050.4	1539.3	Horizontal	Gas permeability, MICP (GCCC)	0.277	25
5051.2	1539.6	Horizontal	Gas permeability, MICP (GCCC)	0.244	45
5053.4	1540.3	Horizontal	Gas permeability, MICP (GCCC)	0.326	2930
5055.1	1540.8	Vertical (V1)	Multistage triaxial loading, N_2-brine injection at in-situ stress condition (Biot coefficient and compressibility), MICP (Our laboratory)	0.376	263
5055.8	1541.0	Horizontal (H1)	Porous plate capillary pressure measurement (Our laboratory)	0.377	-
5055.9	1541.0	Vertical (V2)	Porous plate capillary pressure measurement (Our laboratory)	0.355	-
5061.4	1542.7	Horizontal	Gas permeability, MICP (GCCC)	0.331	1150
5065.6	1544.0	Horizontal	Gas permeability, MICP (GCCC)	0.327	1830
5070.5	1545.5	Horizontal	Gas permeability, MICP (GCCC)	0.280	212
5071.5	1545.8	Horizontal	Gas permeability, MICP (GCCC)	0.353	2650
5075.4	1547.0	Horizontal	Gas permeability, MICP (GCCC)	0.326	1080
5076.3	1547.3	Horizontal	Gas permeability, MICP (GCCC)	0.340	2330

Table 2.3. Measured well log values at depths for shale correction

Property	**Water saturated sands**	**Clay-rich sands**
Depth [m]	1,544 m (5065.5 ft)	4,972.5

Gamma ray [GAPI]	45.5	148.9
Density porosity $\phi_{D,sh}$ [-]	0.354	0.260
Neutron porosity $\phi_{N,sh}$ [-]	0.348	0.501

Table 2.4. Rock types applied to Frio reservoir modeling for capillary pressure and relative permeability. (Assumed parameters include $k_{rnw} = 0.82$ and $S_m = 1$)

Property	**Tight**	**Medium**	**Coarse 1**	**Coarse 2**
Permeability [mD]	0.3	618	1026	2107
Porosity [-]	0.1	0.24	0.29	0.36
J-function	1	2	3	3
λ	0.29	1.1	2	1.9
Pc[MPa]	0.0055	0.0021	0.0028	0.0016
Swirr	0.5	0.279	0.263	0.263

References

Bjerrum, L., Kennard, R. M., Gibson, R. E., and Nash, J. 1972. Hydraulic fracturing in field permeability testing. *Geotechnique*, Vol. 22, Iss. 2, pp. 319-332.

Bauer, S. J., Huang, K., Chen, Q., Ghassemi, A., and Barrow, P. 2016. Experimental and Numerical Investigation of Hydro-Thermally Induced Shear Stimulation. 50 U.S. Rock Mechanics/Geomechanics Symposium, Houston, Texas, 26-29 June.

Delshad, M., Kong, X., & Wheeler, M. F. 2011. On Interplay of Capillary, Gravity, and Viscous Forces on Brine/CO_2 Relative Permeability in a Compositional and Parallel Simulation Framework. Presented at the SPE Reservoir Simulation Symposium, The Woodlands, Texas, 21-23 February. SPE-142146-MS.

Delshad, M., Thomas, S. G. and Wheeler, M. F. 2011. Parallel Numerical Reservoir Simulations of Nonisothermal Compositional Flow and Chemistry. *Society of Petroleum Engineers*, 118847-PA, Vol. 16,

Doughty, C., Freifeld, B. M., Trautz, R. C. 2008. Site characterization for CO_2 geologic storage and vice versa: the Frio brine pilot, Texas, USA as a case study. Environmental Geology, Vol. 54, Iss 8, pp. 1635-1656.

Ehlig-Economides, C. and Economides, M. J. 2010. Sequestering carbon dioxide in a closed underground

volume. *Journal of Petroleum Science and Engineering*, Vol. 70, Iss 1-2, pp. 123-130.

Ellsworth, W. L. 2013. Injection-Induced Earthquakes. Science, Vol. 341 Iss 6142, pp 1225942

Espinoza, D. N., and Santamarina J. C. 2010. Water-CO_2-mineral systems: Interfacial tension, contact angle, and diffusion—Implications to CO_2 geological storage, *Water Resources Research*, Vol. 46, Iss. 7, pp. 1-10.

Frohlich, C. 2012. Two-year survey comparing earthquake activity and injection-well locations in the Barnett Shale, Texas, Proceedings of the National Academy of Sciences of the United States of America, Vol. 109, Iss 35, pp 13934-13938

Hovorka, S. D., Holtz, M. H., Sakurai, S., and others 2003. Report to the Texas Commission on Environmental Quality to Accompany a Class V Application for an Experimental Technology Pilot Injection Well: Frio Pilot in CO_2 Sequestration in Brine-Bearing Sandstones.

Hovorka, S. D., Doughty, C., Benson, S. M., Pruess, K., and Knox, P. R. 2004. The impact of geological heterogeneity on CO_2 storage in brine formations: a case study from the Texas Gulf Coast. *Geological Society*, London, Special Publications, Vol. 233, pp. 147-163.

Hovorka, S. D., C. Doughty, S. M. Benson, and others 2006. Measuring permanence of CO_2 storage in saline formations: The Frio experiment. *Environmental Geosciences*, Vol. 13, Iss. 2., pp. 105–121.

Kharaka, Y. K., Cole, D. R., Hovorka, S. D., and others 2006. Gas-water-rock interactions in Frio Formation following CO_2 injection: Implications for the storage of greenhouse gases in sedimentary basins. *Geology*, Vol. 34, Iss. 7, pp. 577-580.

Kim, J., Tchelepi, H. A., Juanes, R. 2011. Stability, accuracy, and efficiency of sequential methods for coupled flow and geomechanics. *Society of Petroleum Engineers*, Vol. 16, Iss. 02, pp 249-262.

Kong, X., Delshad, M., and Wheeler, M. F. 2015. History Matching Heterogeneous Coreflood of CO_2/brine by Use of Compositional Reservoir Simulator and Geostatistical Approach. *Society of Petroleum Engineers*, Vol. 20, Iss. 2, 267-276.

Nikolinakou, M. A., Flemings, P. B., and Hudec, M. R. 2013. Modeling stress evolution around a rising salt diaper. *Marine and Petroleum Geology*, Vol. 51, pp. 230-238.

Mikelic, A. and Wheeler, M. F. 2013. Convergence of iterative coupling for coupled flow and geomechanics. *Computational Geosciences*, Vol. 17, Iss. 03, pp 455-461.

Rachford, H.H., Rice, J.D. 1952. Procedure for the use of electronic digital computers in calculating flash vaporization hydrocarbon equilibrium. *Society of Petroleum Engineers*. Vol. 4, Iss 10, pp 327-328

Rutqvist, J., Rinaldi, A. P., Cappa, F., Jeanne, P., Mazzoldi, A., Urpi, L., Guglielmi Y. & Vilarrasa, V. (2016). Fault activation and induced seismicity in geological carbon storage–Lessons learned from recent modeling studies. *Journal of Rock Mechanics and Geotechnical Engineering*, Vol. 8, Iss 6, pp 789-804

Sakurai, S., Ramakrishnan, T. S., Boyd, A., Mueller, N., and Hovorka, S. D. 2006. Monitoring Saturation

Changes for CO_2 Sequestration: Petrophysical Support of the Frio Brine Pilot Experiment. *Society of Petrophysics and Well Log Analysis*, Vol. 47, Iss. 6, pp. 483-496.

Settari, A. and Maurits, F. 1998. A coupled reservoir and geomechanical simulations system. *Society of Petroleum Engineers*, Vol. 3, Iss. 2, pp. 219-226.

Singh, G. and Wheeler, M. F. 2016. Compositional Flow Modeling using a Multipoint Flux Mixed Finite Element Method. *Computational Geosciences*, Vol. 20, pp. 421-435.

Torres-Verdin, C. 2016. Integrated Geological-Petrophysical Interpretation of Well Logs. Course Notes of Fundamentals of Well Logging, The University of Texas at Austin

Wheeler, J.A., Wheeler, M.F. and Yotov, I. 2002. Enhanced Velocity Mixed Finite Element Methods for Flow in Multiblock Domain. Computational Geosciences, Vol. 6, Iss. 3, pp 315-332.

Zoback, M. D. and Gorelick, S. M. 2012. Earthquake triggering and large-scale geologic storage of carbon dioxide. *Proceedings of the National Academy of Sciences,* Vol. 109, Iss. 26, pp. 10164-10168

Zoback, M. D. 2007. Reservoir geomechanics. Cambridge: Cambridge University Press.

Task 3.0 Upscale by Completing Bridge from Laboratory to Field Scales

We developed an adaptive homogenization approach upscaling non-linear multiphase flow and transport. A two-phase oil-water problem is considered here that has been extended to handle two-phase air-water type system required for CO_2 sequestration in subsurface aquifers. The workflow of our adaptive homogenization framework has three key steps:

1. Local numerical homogenization to obtain permeability values at the coarse scale by solving local unit-cell problems assuming single phase incompressible flow with periodic boundary conditions.
2. Evaluate an adaptivity criteria for identifying the location of the front and mark transient and non-transient regions.
3. Once the property data (permeability, porosity, etc.) is available at the coarse scale, an AMR scheme is used to solve the coupled transient (fine scale) and non-transient (coarse scale) flow and transport problems.

Local Numerical Homogenization

The local numerical homogenization step involves solving auxiliary problems over a subdomain Ω_i at a given fine scale to obtain an effective value of permeability, porosity or dispersion at a chosen coarse scale. Here, local is used to refer to the subdomains over which the auxiliary problems are solved using periodic boundary conditions for each subdomain. Figure 3.1 shows a schematic of the local numerical homogenization with the fine scale auxiliary problem (dotted red, left) to obtain coarse scale effective values (dotted red, right).

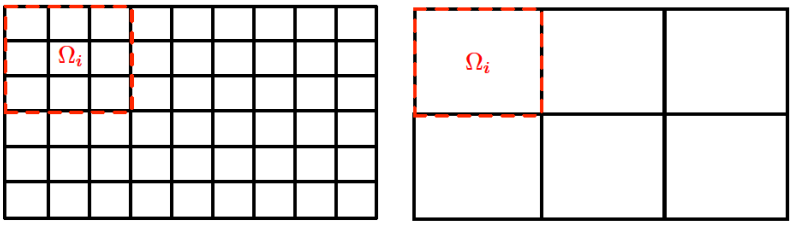

Figure 3.1 Schematic of local numerical homogenization to obtain coarse scale (right) prarameters from fine scale (left)

Oversampling

Although the local numerical homogenization with non-overlapping subdomains provides good estimates for effective properties at the coarse scale, for some channelized cases this might result in loss of channel connectivity. This issue has been identified by several others; (Efendiev and Hou, 2009; Chung et al., 2016) to cite a few, and has been addressed by using overlapping subdomains during the evaluation of multiscale basis. In this work, we use the same approach wherein subdomains are allowed to overlap over a predefined (or user specified) region. Figure 3.2 shows a schematic of oversampling for local numerical homogenization with overlapping subdomains. The effective properties are then evaluated by solving a local numerical homogenization over these extended subdomains.

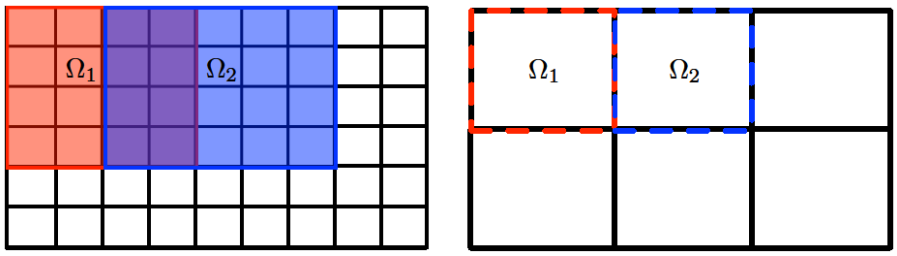

Figure 3.2: Oversampling for local numerical homogenization

We observe improvements in numerical solution accuracy of our adaptive approach; compared to the fine scale solution, for channelized permeability distributions with fine (or thin) high permeability streaks. This oversampling approach does not affect our overall computational efficiency since local numerical homogenization is performed only once prior to a numerical simulation for a given set of reservoir property distribution.

Adaptivity Criterion

We now require an indicator function to track the location of the saturation front in order to later perform a domain decomposition into transient and non-transient regions. An ad hoc criterion for identifying the location of the saturation front can be easily defined using a gradient in saturation between saturation at a given point in space and its nearest neighbor. One such criterion is using a maximum of absolute of difference between a saturation S at an element and its adjacent elements at the previous time step n. We define the neighboring elements collectively as, $\Omega_{neighbor}(x)=\{y:y\in E_j,|\partial E_i\cap\partial E_j|\neq\varnothing,if x\in E_i\}$.Then the adaptivity criteria can be written as,

$$\Omega_f = \{x : \max|c^n(x) - c^n(y)| > \varepsilon_{adap} \ \forall y \in \Omega_{neighbor}(x)\}$$

Here, E_i and E_j represent an element and its neighbors with ε_{adap} as the threshold value above which a domain is marked as a transient region. Please note that this type of adaptivity criterion has been used by others (Aarnes and Efendiev, 2006) to reduce computational costs in a similar sense. However, the computational speedup obtained in the former is not clear. Such criteria have been used in the past for different problems as well. For example, in compositional flow modeling (Singh and Wheeler, 2016), the local equilibrium computations (flash calculations) are performed based upon the identification of a spatial transient region where a given fluid composition was unstable at a previous timestep.

Adaptive Mesh Refinement

Based upon the above criteria we divide the domain (Ω) into non-overlapping, transient (Ω_f) and non-transient (Ω_c) subdomains to solve flow and transport problems at the fine and coarse scales, respectively. Figure 3.3 shows a schematic of the domain decomposition approach used here. In what follows, coarse and non-transient, and fine and transient can be used interchangeably to refer to a subdomain. The coarse and fine subdomain problems are then coupled at the interface using the EVMFEM spatial discretization described in Wheeler et al. (2002). The EV MFE method is known to be strongly mass conservative at the interface between fine and coarse domains. Further, this scheme has been used previously; as a multiblock domain decomposition approach, for a number of fluid flow and transport problems (Thomas and Wheeler, 2011) including EOS compositional flow. This adaptive homogenization approach has also been used for upscaling single phase, slightly compressible flow, and tracer transport in Amanbek et al.

(2017). Here, the EV MFE was used as the multiblock, domain decomposition approach similar to its usage in this work.

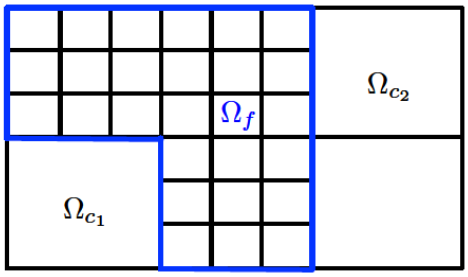

Figure 3.3: Schematic of adaptive mesh refinement with coarse (Ω_c) and fine (Ω_f) domains.

Solution Algorithm

In this section, we discuss the numerical solution algorithm with a brief description of spatial and temporal discretizations employed. We assume that the oil phase pressure p_o and saturation S_o are the primary unknowns to form the non-linear system of algebraic equations representing the weak form of the two-phase flow model formulation. The lowest order (RT0) mixed finite element method (Arbogast et al., 1997) ; equivalent to the finite difference scheme, is used for spatial discretization with a backward Euler scheme for temporal discretization. A Newton linearization is then performed to obtain a linear system of algebraic equations hence resulting in a fully implicit solution scheme.

Algorithm 1 Workflow for adaptive numerical homogenization

Solve unit-cell problems, Eqns. (9), on subdomains (Ω_i) using fine scale parameters to obtain coarse scale parameters for the entire domain ($\Omega = \cup\Omega_i$, see Figure 3).

while $t_n \leq T$ **do**

Identify transient (Ω_f) and non transient (Ω_c) regions using adaptivity criteria Eqn. (10) and p_o, S_o at t_n ($\Omega_f \cup \Omega_c = \Omega$).

Mass conservative initialization of primary unknowns:

1. Reconstruct primary unknowns $p_o^{n+1,0}, S_o^{n+1,0}$ for the fine scale transient region (Ω_f).
2. Project primary unknowns $p_o^{n+1,0}, S_o^{n+1,0}$ for the coarse scale non-transient region (Ω_c).

while $max(\vec{R}_{nl}) > \varepsilon_{nl}$ **do**

1. Use fine and coarse scale parameters in the transient (Ω_f) and non-transient (Ω_c) regions, respectively.
2. Use enhanced velocity (EV) scheme to couple coarse and fine subdomains.
3. Solve linearized, algebraic system for the coupled flow and transport problem to obtain a Newton update $p_o^{n+1,k+1}, S_o^{n+1,k+1}$.

$k := k+1$

end

$t_{n+1} = t_n + \Delta t$, $n := n+1$

end

Algorithm 1 presents the solution algorithm for the adaptive homogenization approach. Here, n and k are the time and non-linear iteration counter, t_n and t_{n+1} are the current and next time, Δt current time-step size, T the final time, $\max(\vec{R}_{nl})$ the max norm of the non-linear residual vector, and ε_{nl} the non-linear tolerance. The adaptivity criteria (10) is evaluated at the coarse scale; for each time step, to identify the transient region for the next time step. Once identified the reservoir domain is divided into fine (Ω_f) and coarse Ω_c subdomains. A fully coupled, monolithic construction of the multiblock domain decomposition approach EV MFEM is then used for coupling non-matching coarse and fine subdomains. The coupled monolithic construction is an improvement over the previous implementations of the EV MFEM (Wheeler et al., 2002; Thomas and Wheeler, 2011) approach where the interface contributions are neglected. This approach was also used for upscaling single-phase flow and tracer transport earlier by (Amanbek et al., 2017). The non-linear iterations are performed until the max norm ($\max(\vec{R}_{nl})$) satisfies a desired tolerance (ε_{nl}) corresponding to the error in phase mass conservation equations.

Numerical Results

In this section, we present numerical experiments beginning with verification cases for numerical homogenization and AMR using periodic and homogeneous reservoir properties, respectively for the two cases. Next we demonstrate the capability of our adaptive homogenization approach using reservoir property description from different horizontal layers of the 10^{th} SPE comparative project for upscaling approaches (Christie and Blunt, 2001). We specifically rely upon two layers of the SPE10 project: (1) layer 20 with a near Gaussian distribution of permeability, and (2) layer 38 with layered or highly channelized permeability distribution. These contrasting cases are aimed to test the solution accuracy and computational efficiency of our adaptive homogenization approach compared to a fine scale solve over the entire reservoir domain. The reservoir domain is 220ft×60ft with coarse and fine scale grid discretizations of 22×6 and 220×60, respectively. The coarse and fine grid elements are consequently 10ft×10ft and 1ft×1ft. The fluid and reservoir properties are mostly taken from the SPE10 dataset with minor modifications to oil phase compressibility to fit the two-phase flow model formulation. The oil and water phase compressibility is taken to be 1×10^{-4} and 3×10^{-6} psi^{-1}, respectively. Further the fluid viscosities is assumed to be 3 and 1 cP for the oil and water phases, respectively. Additionally, a Brook's Corey model, is considered for the two-phase relative permeabilities with endpoints $S_{or} = S_{wirr} = 0.2$ and $k_r^0{}_o = k_r^0{}_w = 1.0$, and model exponents $n_o = n_w = 2$, as suggested in the SPE10 dataset.

In all of the following numerical cases, the initial reservoir pressure and saturation are taken to be 1000 psi and 0.2, respectively. Further, the injection well is water-rate specified at 2 STB/day whereas the production well is pressure specified at 1000 psi. All numerical simulations are carried out for a total of 200 days with continuous water injection. Please note that although a homogeneous dataset is provided in SPE10 data for relative permeability and capillary pressure, our upscaling approach is not restrictive in this sense. In fact, for such heterogeneities an average relative permeability and capillary pressure can be obtained at the coarse scale; following the two-scale homogenization work of Bourgeat et al. (2003). However, we do not need to evaluate these effective functions at the coarse scale since we are resolving fine scale features at the front using AMR.

Verification: Homogeneous Case

We verify the adaptivity criteria and AMR using a homogeneous permeability of dis- tribution of 50mD. Figure 3.4 shows the saturation profile after hundred days of continuous water injection. As can be easily

seen from these figures the saturation profiles for the fine and adaptive approaches are in excellent agreement.

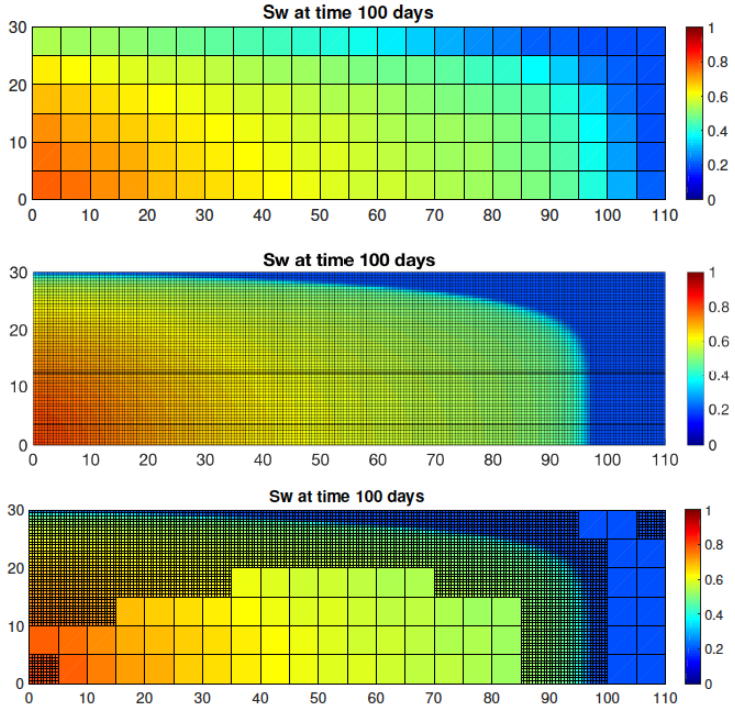

Figure 3.4: Saturation profiles after 100 days for coarse (top), fine (middle), and adaptive (bottom) approaches.

Figures 3.5 and 3.6 further show the oil rate and cumulative oil at the production well, respectively. These results further bolster the fact that the AMR with the proposed adaptivity criteria provides an accurate solution when compared against the fine scale solution. The coarse scale solution deviates mildly from the other two set of results due to numerical diffusion introduced by the upwinding scheme and coarse grid discretization. The AMR is able to curtail the numerical diffusion introduced by upwinding at the saturation front by using a dynamic fine grid around the saturation front.

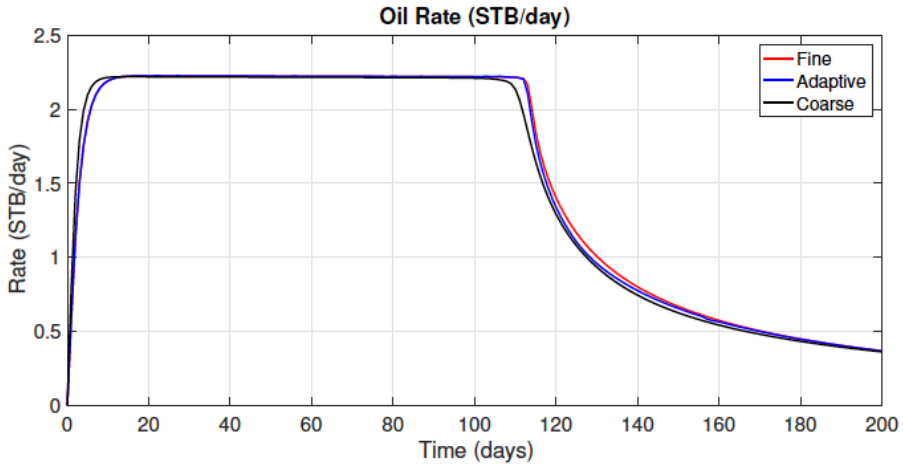

Figure 3.5: Oil rate at production wells (STB/day)

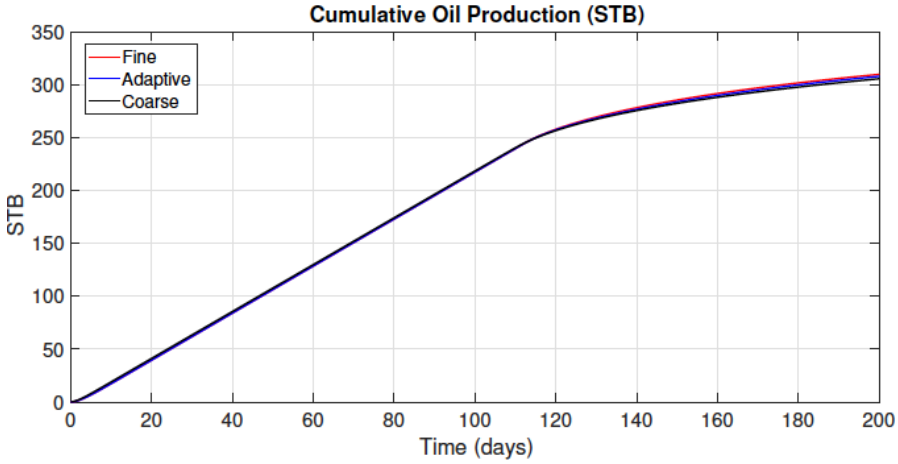

Figure 3.6: Cumulative oil production (STB)

Gaussian Permeability Distribution

For this numerical test, we use layer 20 of the SPE10 dataset that has a relatively Gaussian distribution of permeability. Figure 3.7 shows fine scale permeability distribution; extracted from the dataset, and coarse scale distribution obtained after numerical homogenization. As discussed earlier, this numerical homogenization step to obtain effective properties at the coarse scale is only performed once and does effect the overall computational efficiency.

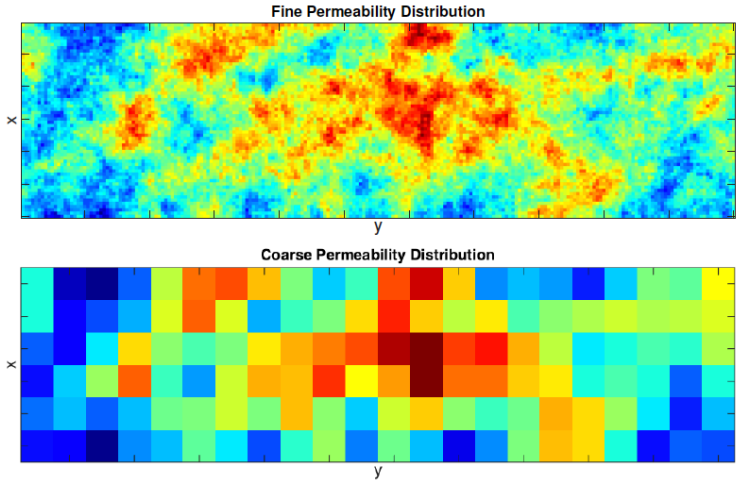

Figure 3.7: Fine and coarse scale permeability distributions for SPE10 layer 20

Figure 3.8 shows the saturation profile after 50 days for the coarse, fine, and adaptive approaches. It is clear from these figures that saturation fronts are captured almost as accurately as the fine scale solution at substantially less computational cost. This is achieved by solving the fine scale problem only in reservoir subdomains where changes in saturation are large; as identified by our adaptivity criteria.

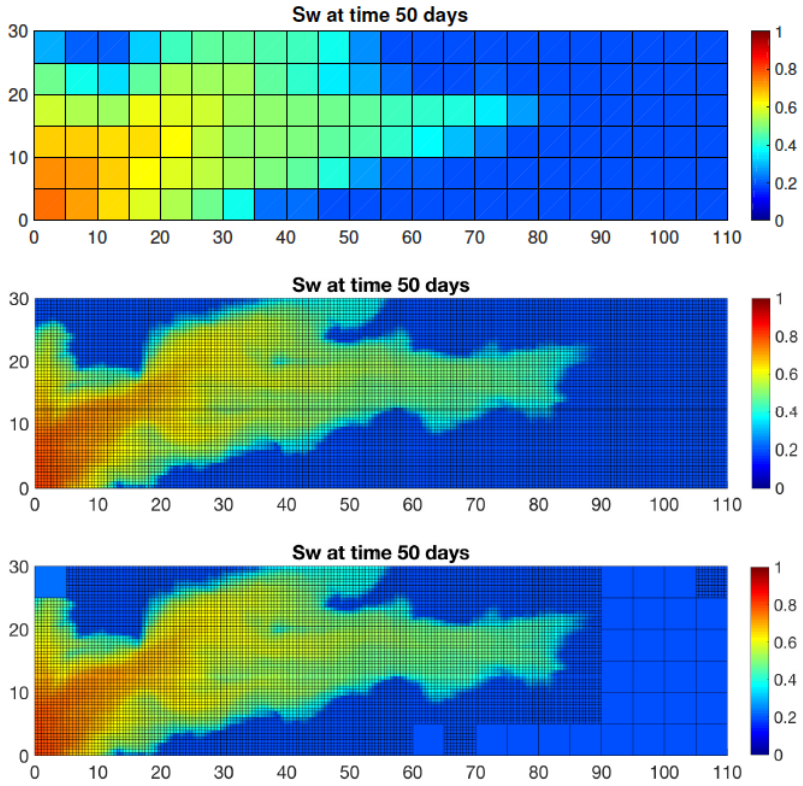

Figure 3.8: Saturation profiles after 50 days for coarse (top), fine (middle), and adaptive (bottom) approaches.

Figures 3.9 and 3.10 show the oil rate and cumulative oil at the production well. These figures clearly show that the adaptive approach is again in excellent agreement with the fine scale solution for the Gaussian permeability distribution under consideration. Again, this is more or less expected since the permeability distribution is Gaussian in nature and therefore has some ergodicity; or periodic properties in a statistical paradigm. Therefore the basic assumptions of two-scale homogenization theory and consequently local numerical homogenization are inherently valid.

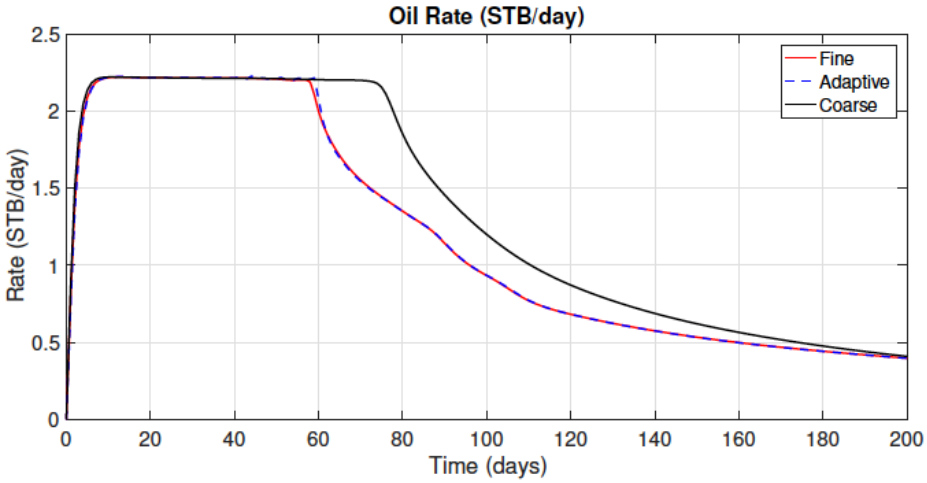

Figure 3.9: Oil rate at production well (STB/day) for layer 20 of SPE10.

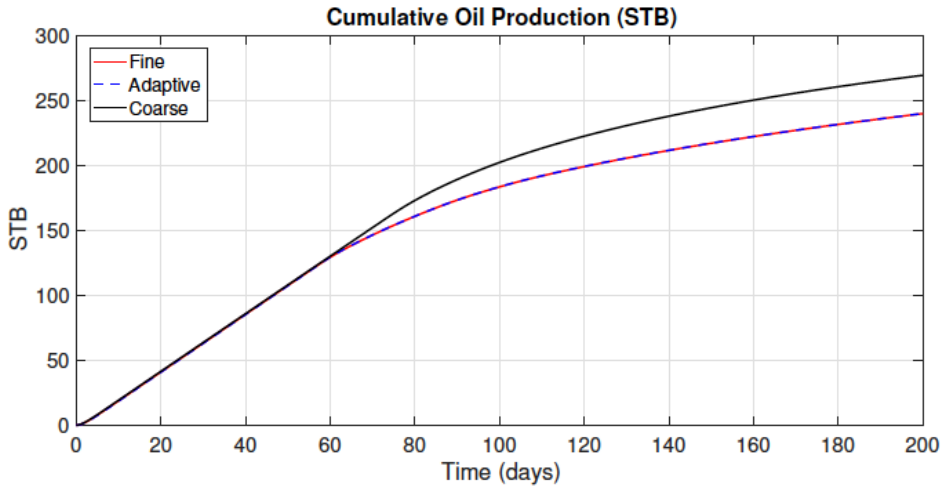

Figure 3.10: Cumulative oil production (STB) for layer 20 of SPE10.

Channelized Permeability Distribution

Next, we consider layer 38 of the SPE10 dataset that has a channelized or layered permeability distribution with stark contrast in permeability values. Figure 3.11 shows fine scale permeability distribution and coarse scale distribution obtained after numerical homogenization; similar to the previous numerical test case. This figure clearly shows that channels connectivity is lost in the coarse scale permeability distribution obtained from local numerical homogenization.

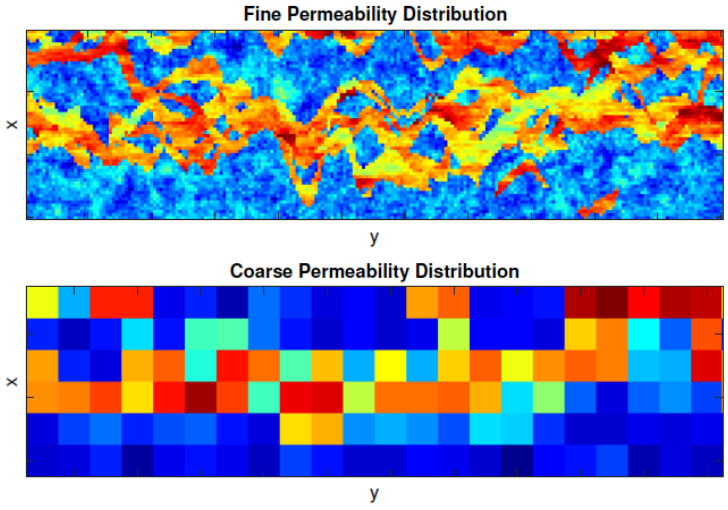

Figure 3.11: Permeability distribution at fine (top) and coarse (bottom) scale from SPE 10 layer 38.

We are able to recover connectivity using oversampling to some extent however, we still observe a substantial deviation in solution accuracy for the coarse scale. However, our adaptive homogenization approach is still able to recover fine scale features as can be seen from the saturation profile in Figure 3.12.

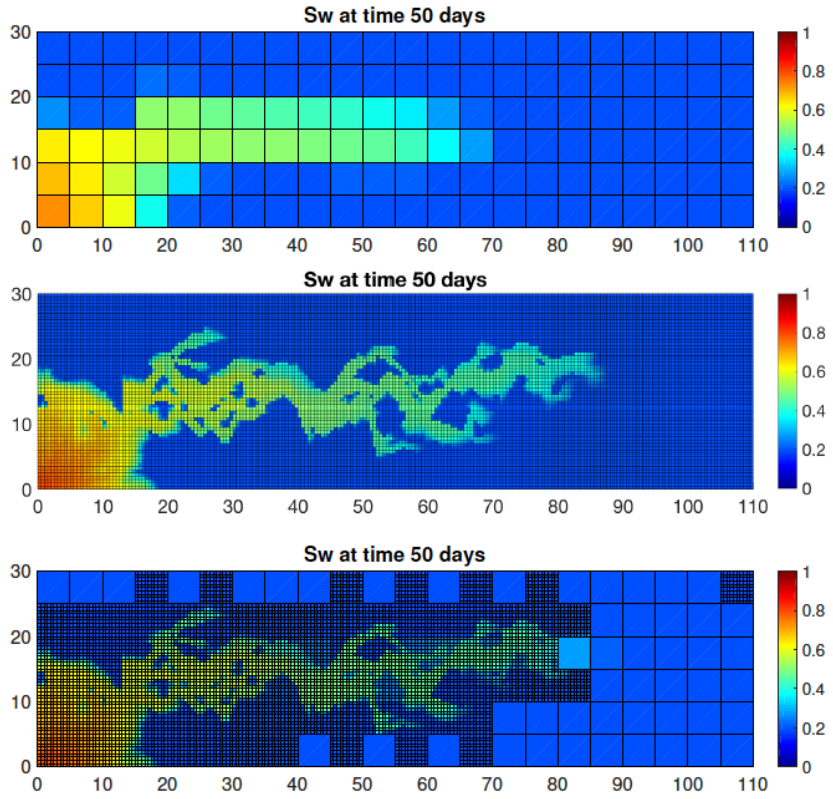

Figure 3.12: Saturation profiles after 50 days for coarse (top), fine (middle), and adaptive (bottom) approaches.

Figures 3.13 and 3.14 show the oil rate and cumulative oil at the production well. The deviation of the oil rate for the adaptive case (spikes) can be improved by tightening the adaptive criteria, however this results in additional computational overheads. Since the cumulative oil production is already a good match we did not consider this aforementioned approach to resolve the oil-rates better.

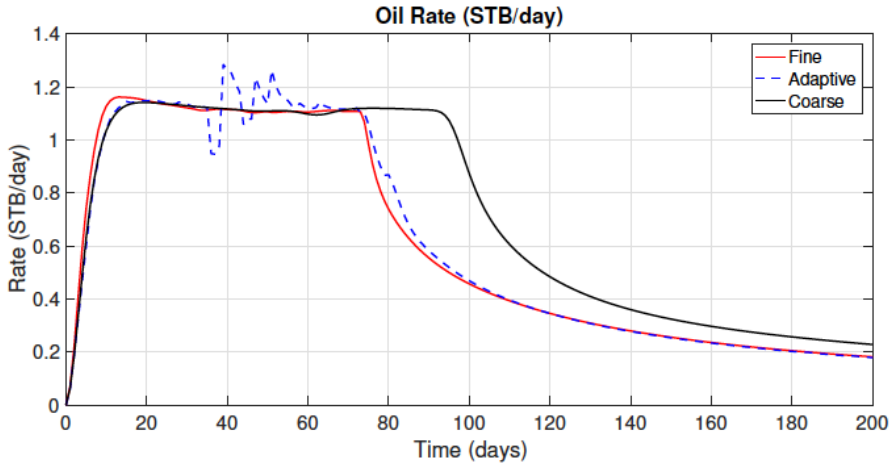

Figure 3.13: Oil rate at production well (STB/day) for layer 38 of SPE10.

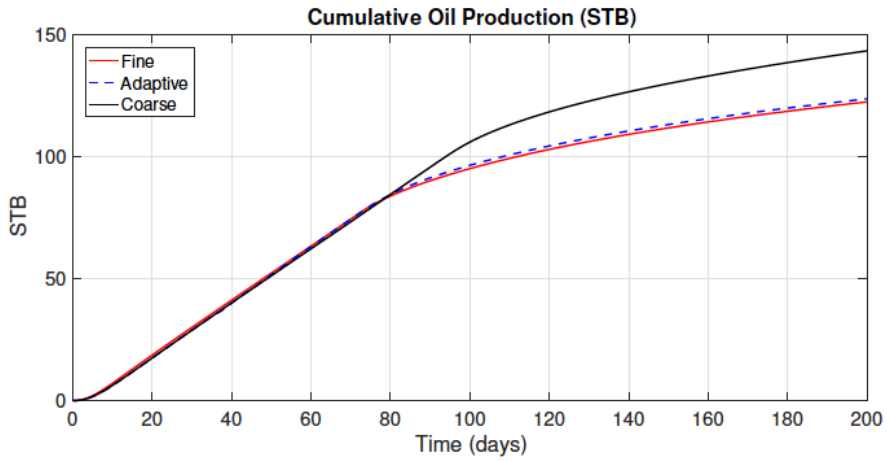

Figure 3.14: Cumulative oil production well (STB) for layer 38 of SPE10.

An adaptive numerical homogenization approach is reported that relies upon identifying characteristic flow features; such as the saturation front, and resolving them at the fine scale for accuracy. The computational efficiency is achieved by solving a coarse scale problem away from the saturation front with effective coefficients; obtained from one time local numerical homogenization for a given reservoir property distribution, at the coarse scale. An oversampling technique for the local numerical homogenization step preserves connectivity of channels; across coarse subdomains, in a layered permeability medium. Further, a non-linear preconditioning approach was developed to reduce the number of non-linear iterations improving the computational efficiency of the overall approach for a multiphase flow system. The numerical results indicate that the solutions obtained using our adaptive homogenization approach are in good agreement with the fine scale solutions. The breakthrough times and production histories are predicted more accurately compared to a purely coarse scale; using local numerical homogenization without AMR, solve. We obtain a speedup of approximately 4 times for all our numerical test cases since the saturation front; where a fine scale solution is required, occupies only a small subdomain of the entire reservoir. Further speedups can be obtained by using a loose adaptivity criteria at the cost of solution accuracy. This approach can be easily extended to black-oil, compositional (gas and chemical flooding), and reactive flow type systems with a some modifications in local numerical homogenization and non-linear preconditioning steps. As mentioned previously, the effective equations; using two-scale homogenization, for different flow models share common workflow elements that do not change with the flow model under consideration. Thus adaptive homogenization is a general upscaling framework with a certain degree of process independence.

References

Aarnes, J. E. and Efendiev, Y., 2006. An adaptive multiscale method for simulation of fluid flow in heterogeneous porous media. Multiscale Modeling & Simulation, 5 (3): 918–939.

Allaire, G., 1992. Homogenization and two-scale convergence. SIAM Journal on Mathematical Analysis, 23 (6): 1482–1518. Amanbek, Y., Singh, G., Wheeler, M. F., and van Duijn, H., 2017. Adaptive numerical homogenization for upscaling single

phase flow and transport. ICES Report, 12 (17). Amaziane, B., Bourgeat, A., and Jurak, M., 2006. Effective macrodiffusion in solute transport through heterogeneous porous media. Multiscale Modeling &

Simulation, 5 (1): 184–204. Arbogast, T., 2012. Mixed Multiscale Methods for Heterogeneous Elliptic Problems, 243–283. Springer Berlin Heidelberg,

Berlin, Heidelberg. Arbogast, T., Pencheva, G., Wheeler, M. F., and Yotov, I., 2007. A multiscale mortar mixed finite element method. Multiscale

Modeling & Simulation, 6 (1): 319–346. Arbogast, T., Wheeler, M., and Yotov, I., 1997. Mixed finite elements for elliptic problems with tensor coefficients as cell-centered finite differences. SIAM J. Numer. Anal., 32 (2): 828–852.

Bear, J., 1972. Dynamics of fluids in porous media. Textbook.

Bensoussan, A., Lions, J.-L., and Papanicolaou, G., 1978. Asymptotic analysis for periodic structures, volume 5. North- Holland Publishing Company Amsterdam.

Bourgeat, A., Jurak, M., and Piatnitski, A. L., 2003. Averaging a transport equation with small diffusion and oscillating velocity. Mathematical Methods in the Applied Sciences, 26 (2): 95–117.

Brooks, R. and Corey, A., 1964. Hydraulic properties of porous media. Hydrology Papers No. 3, 26 (2).

Buckley, S. and Leverett, M., 1942. Mechanism of fluid displacement in sands. SPE Journal, 146 (01).

Christie, M. A. and Blunt, M. J., 2001. Tenth spe comparative solution project: A comparison of upscaling techniques. SPE Reservoir Evaluation and Engineering, 4 (04).

Chung, E., Efendiev, Y., and Hou, T. Y., 2016. Adaptive multiscale model reduction with generalized multiscale finite element methods. Journal of Computational Physics, 320: 69–95.

Dawson, C. N., Klie, H., Wheeler, M. F., and Woodward, C. S., 1998. A parallel, implicit cell-centered method for two-phase flow with a preconditioned newton-krylov solver. Computational Geosciences, 1 (3): 215–249.

Durlofsky, L. J., 2003. Upscaling of geocellular models for reservoir flow simulation: A review of recent progress. In 7 th International Forum on Reservoir Simulation. Citeseer.

Efendiev, Y. and Hou, T. Y., 2009. Multiscale finite element methods: theory and applications, volume 4. Springer Science & Business Media.

Eisenstat, S. C. and Walker, H. F., 1994. Globally convergent inexact newton methods. SIAM Journal of Optimization, 4 (2): 393–422.

Farmer, C. L., 2002. Upscaling: a review. International Journal for Numerical Methods in Fluids, 40 (1): 63–78. Genuchten, V., 1980. A closed-form equation for predicting the hydraulic conductivity of unsaturated soils. Soil Science

Society of America Journal, 44 (5): 892–898. Jikov, V. V., Kozlov, S. M., and Oleinik, O. A., 2012. Homogenization of differential operators and integral functionals. Springer Science & Business Media.

John, A. K., 2008. Dispersion in Large Scale Permeable Media. Ph.D. thesis, The University of Texas at Austin.

Mikelic, A., Devigne, V., and Van Duijn, C., 2006. Rigorous upscaling of the reactive flow through a pore, under dominant peclet and damkohler numbers. SIAM journal on mathematical analysis, 38 (4): 1262–1287.

Singh, G. and Wheeler, M. F., 2016. Compositional flow modeling using a multi-point flux mixed fi- nite element method. Computational Geosciences, 20 (3): 421–435. doi:10.1007/s10596-015-9535-2. URL http://dx.doi.org/10.1007/s10596-015-9535-2.

Tavakoli, R., Yoon, H., Delshad, M., ElSheikh, A. H., Wheeler, M. F., and Arnold, B. W., 2013. Comparison of ensemble filtering algorithms and null-space monte carlo for parameter estimation and uncertainty quantification us- ing co2 sequestration data. Water Resources Research, 49 (12): 8108–8127.

Thomas, S. G. and Wheeler, M. F., 2011. Enhanced velocity mixed finite element methods for modeling coupled flow and transport on non-matching multiblock grids. Computational Geosciences, 15 (4): 605–625.

Wheeler, J. A., Wheeler, M. F., and Yotov, I., 2002. Enhanced velocity mixed finite element methods for flow in multiblock domains. Computational Geosciences, 6 (3-4): 315–332.

Wu, X.-H., Efendiev, Y., and Hou, T. Y., 2002. Analysis of upscaling absolute permeability. Discrete and Continuous Dynamical Systems Series B, 2 (2): 185–204.

Task 4 - Simulator Development and Modeling CO_2 Storage Field Scale Studies

Coupled Compostional Flow and Elastoplasticity Model

An extensive amount of work has been done previously (Delshad et al, 2013) on modeling and numerical simulation of CO_2 sequestration for Cranfield, using an EOS compositional flow model in the house reservoir simulator IPARS, by one of the co-PIs. However, most of these prior studies did not include the effect of reservoir geomechanics on the field integrity and storage capacity. The modeling work presented in this report accounts for the elastoplastic nature of the reservoir rock by considering a Drucker-Prager plasticity model. An independent experimental study was conducted by one of the co-PIs (in the Laboratory Experiments section below) to determine rock properties, from Cranfield cores, for both flow and geomechanics. The main objective of this combined experimental and numerical study is to quantify the impact of mechanical deformation, either elastic or plastic, on reservoir integrity, to identify and optimize operational choices for any long-term CO_2 sequestration field project.

As a part of the modeling and simulation task, we integrated an implementation of the Drucker-Prager plasticity model into the parallel compositional reservoir simulator, IPARS (Integrated Parallel Accurate Reservoir Simulator). Fluid flow is formulated on general distorted hexahedral grids using the multipoint flux mixed finite element method. The mechanics and flow systems are solved separately and coupled using a fixed-stress iterative coupling algorithm. This allows multiple flow models to be used with nonlinear mechanics without modification, and allows each type of physics to use appropriate preconditioners for its linear systems. The fixed-stress iteration converges to the fully coupled solution on each time step. With these components in place, we conduct a study on wellbore stability using different flow and geomaterial models. Our simulations run efficiently in parallel using MPI on high performance computing platforms up to hundreds or thousands of processors.

The coupled poro-elasto-plasticity system consists of a Drucker-Prager elasto-plasticity model coupled with a number of different fluid flow model options, including an Equation of State Compositional Flow model. The mechanics model is discretized using a Continuous Galerkin (CG) finite element method, and the flow models are discretized using a multipoint flux mixed finite element (MFMFE) method (Singh et al, 2016). Both types of physics are resolved on the same distorted hexahedral grid. Our models were implemented in the IPARS (Integrated Parallel Accurate Reservoir Simulator) code, developed at the Center for Subsurface Modeling at UT Austin. The reader is referred to (White el al, 2017), one of our recent publication, for more details regarding model formulation and the solution algorithm for the non-linear plasticity solution algorithm. The numerical simulations for the coupled compositional flow and geomechanics indicate substantial differences in CO2 plume migration and near wellbore deformations between elastic and plastic models.

In this example, real data is used from the CO2 sequestration demonstration project at the Cranfield reservoir in Mississippi to demonstrate our poro-elasto-plastic model implementation on a large-scale case in parallel on a high-performance computing platform. The domain size is $440 \times 9400 \times 8800$ [ft3] at a depth of 9901 [ft] discretized into a hexahedral grid of $26 \times 188 \times 176$ elements. The reservoir formation is 80 [ft] thick and slopes downward at an angle between 1 and 3 degrees. We used the reservoir depth information to generate the hexahedral grid padded with 3 layers of overburden and 3 layers of underburden, so that all faces of the domain become flat and are more amenable to the application of boundary conditions on the geomechanical system. In Figure 15 we show plots of the history-matched heterogeneous porosity and permeability fields (x-component shown), as well as a close-up of the hexahedral mesh. In the overburden and underburden layers, the porosity is $\phi = 0.05$ and the permeability is $K = 0$ [md].

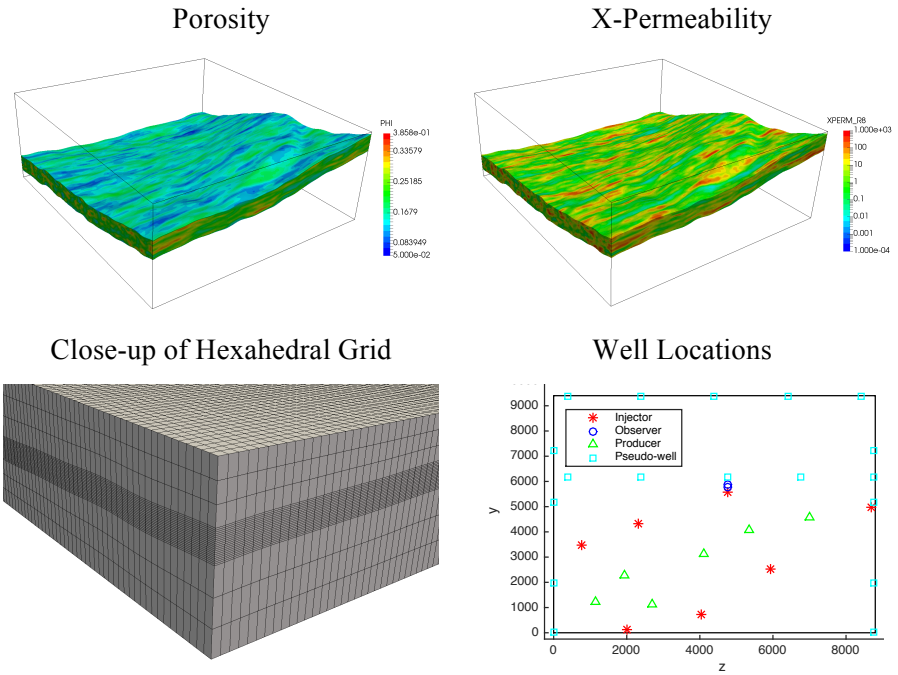

Figure 15. Schematic of numerical reservoir model for Cranfield

The compositional model parameters are calibrated for $N_c = 2$ components, namely "CO2" and "brine". Compositional parameters for the two components include: critical temperatures {547.56, 1120.23}, critical pressures {1070.3785, 3540.8836}, critical volumes {0.30234, 0.22983}, acentric factors {0.2240, 0.2440}, molecular weights {44.01, 18.0125}, parachor {49.0, 52.0}, volumetric shift {-0.19, 0.065}, and binary interaction coefficients -0.009 between each component. Water properties are viscosity $\mu_w = 0.7$

[cp], compressibility $c_w = 3.3\text{E-}6$ [1/psi], and standard density $\rho_{w,std} = 62.4$ [lb/ft3]. In Table 2, relative permeability and capillary pressure are given as piecewise linear functions. The initial hydrostatic reservoir pressure is $p = 4650$ [psi] with 100% brine composition at a temperature of 125°C, and no-flow boundary conditions are used. This reservoir model has 33 vertical wells which are completed in the reservoir formation: 7 mass rate specified gas injection wells, 8 total reservoir volume rate specified production wells, 2 observation wells, and 18 pressure specified pseudo-wells to simulate boundary conditions. Well rates are used from field data. Our simulation is isothermal, with dispersion turned off, and gravitational force turned on. Rock density is 2.65 [gm/cm3]. The end simulation time is T=595 [day], and adaptive time steps are used such that $\Delta t \in (0.001, 1.0)$ [day].

Table 2. From left to right: oil relative permeability versus water saturation, water relative permeability versus water saturation, oil relative permeability versus gas saturation, gas relative permeability versus gas saturation, gas-oil capillary pressure versus gas saturation, oil-water permeability versus water saturation

Sw	Kro	Sw	Krw	Sg	Kro	Sg	Krg	Sg	Pcgo	Sw	Pcow
0.2	1.0	1.0	0.2500	0	0.65	0.05	0.	0.4	100.	0.2	45.0
0.2899	0.6769	0.9	0.1640	0.025	0.65	0.075	0.0001	0.425	0.9238	0.2899	19.03
0.3778	0.4153	0.8	0.1024	0.05	0.65	0.1	0.0011	0.45	0.6554	0.3778	10.07
0.4667	0.2178	0.7	0.0600	0.075	0.5398	0.125	0.0037	0.475	0.5362	0.4667	4.90
0.5556	0.0835	0.6	0.0324	0.1	0.4443	0.15	0.0087	0.5	0.4650	0.5556	1.80
0.6444	0.0123	0.5	0.0156	0.125	0.3621	0.175	0.0165	0.525	0.4164	0.6444	0.50
0.7000	0.0	0.4	0.0064	0.15	0.2918	0.2	0.0279	0.55	0.3805	0.7000	0.05
		0.3	0.0020	0.175	0.2323	0.225	0.0431	0.575	0.3525	0.7333	0.01
		0.2	0.0004	0.2	0.1824	0.25	0.0627	0.6	0.3300	0.8222	0.0
		0.1	0.0000	0.225	0.1410	0.275	0.0868	0.625	0.3113		
				0.25	0.1070	0.3	0.1158	0.65	0.2954		
				0.275	0.0796	0.325	0.1496	0.675	0.2818		
				0.3	0.0578	0.35	0.1884	0.7	0.2699		
				0.325	0.0409	0.375	0.2321	0.725	0.2595		
				0.35	0.0279	0.4	0.2806	0.75	0.2501		
				0.375	0.0183	0.425	0.3338	0.775	0.2417		
				0.4	0.0114	0.45	0.3912	0.8	0.2341		
				0.425	0.0067	0.475	0.4526	0.825	0.2272		
				0.45	0.0036	0.5	0.5175	0.85	0.2208		
				0.475	0.0017	0.525	0.5853	0.875	0.2150		

		0.5 0.0007 0.525 0.0002 0.55 0.0	0.55 0.6555 0.575 0.7273 0.6 0.8	0.9 0.2096 0.925 0.2046 0.95 0.2	

The mechanics boundary conditions are a normal traction of 10054 [psi] on the top face, zero normal displacements on the five remaining faces, and zero shear tractions on all six faces. Material properties are divided into 3 facies with values determined by lab experiments, given in Table 3. Biot's constants are $\alpha = 0.9$ and $1/M = 1.\text{E-}6$ [1/psi]. Plasticity parameters are yield strength $\sigma_Y = 1600$ [psi], yield and flow function slopes of 0.6, and bilinear hardening slope of 3750 [psi].

Table 3. Young's Modulus and Poisson's Ratio for the Cranfield example

Facies	Layers	E [psi]	ν
Overburden	1–3	2.2E6	0.25
C	4–6	1.45E6	0.31
B	7–11	2.68E6	0.26
A	12–23	1.45E6	0.24
Underburden	24–26	2.2E6	0.25

We present simulation results for the Cranfield example in Figure 16. While contour values are only colored in the reservoir layers, note that all simulation values are computed throughout the entire domain. We present these results for the plastic model, although both flow and elastic models were also run. Pressure values were very similar for elastic and plastic cases, and were higher than the flow only case by about 10 [psi]. Displacements were slightly different for elastic and plastic cases, but show the same overall contour. Note the volumetric plastic strain is one order of magnitude smaller than the volumetric strain. These results indicate the model is not extremely sensitive to geomechanical effects with the current set of model parameters. Given the hypothesized geomechanical effects observed in the field when CO2 injection rates were doubled, more model calibration might be necessary.

X-Displacement, t=5 [day] X-Displacement, t=595 [day] Volumetric Strain, t=595 [day]

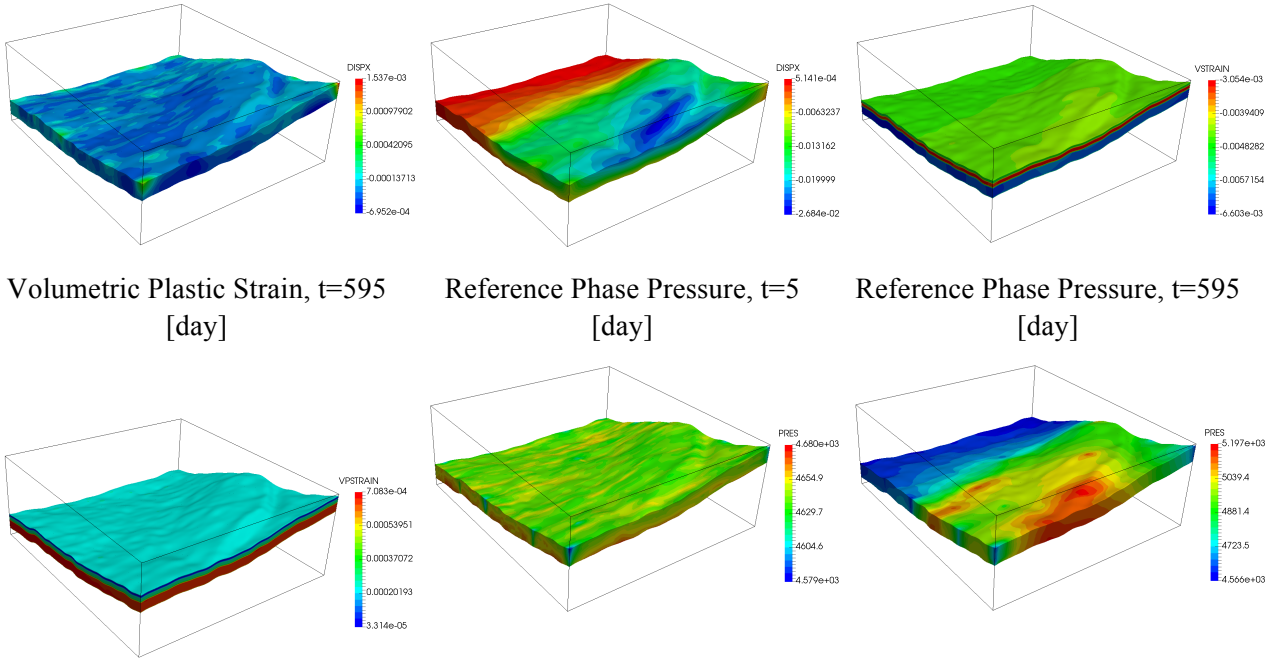

Volumetric Plastic Strain, t=595 [day]

Reference Phase Pressure, t=5 [day]

Reference Phase Pressure, t=595 [day]

Figure 16. Selected simulation results for Cranfield example with plastic model

Hysteretic Relative Permeability and Capillary Pressure Modeling

We verified the implemented multiphase relative permeability (UTKR3P) and multiphase hysteresis (UTHYST) models into IPARS. The UTKR3P model (Beygi et al., 2014) is general (for two or three phases), simple in the sense of practical reservoir simulation, and robust in computational applications. This compositionally-consistent relative permeability model enables to better estimate the fluid mobility at low saturation range where common three-phase relative permeability models cannot fully represent the fluid flow behavior. In addition, the observed inverse S-shape of non-wetting phase (CO2) at high saturation in mixed-wet rocks can be modeled by the UTKR3P model. The parameterized-level model incorporates a saturation-averaged interpolation scheme to evaluate relative permeability parameters (endpoint and curvatures) based on the reference state (measured) parameters. This methodology allows for accurate estimation of relative permeability when saturation history (saturation direction or path) varies in multicycle processes. The residual saturation depends on rock wettability and saturation history.

The UTHYST model (Beygi et al., 2014) enables to capture the trapping behavior of CO_2 as a non-wetting phase during multicycle processes, e.g. huff-n-puff CO_2 injection into aquifers, in water-wet, mixed-wet-, and oil-wet rocks. The memory-dependent trapping is modeled based on the laboratory and field observations. (i) The trapped saturation monotonically increases in the decreasing saturation process and is invariable during the increasing saturation process. If compositional effects lead to remobilize part of the trapped saturation, the non-monotonic trapping behavior will be captured through the capillary desaturation effect. (ii) The Land coefficient by which the initial-trapping behavior is estimated varies

dynamically in multicycle processes. (iii) A conjugate phase saturation impacts the level of phase trapping.

References

Delshad, M., Kong, X., Tavakoli, R., Hosseini, S.A., Wheeler, M.F. Modeling and simulation of carbon sequestration at Cranfield incorporating new physical models. International Journal of Greenhouse Gas Control 18, 463-473, 2013.

Singh, G., and Wheeler, M.F. Compostional flow modeling using a multipoint flux mixed finite element method. Computational Geosciences 20 (3), 421-435, 2016.

White, D., Ganis, B., Liu, R., and Wheeler, M.F. A near-wellbore study with a Drucker-Prager plasticity model coupled with a parallel compositional reservoir simulator, SPE Reservoir Simulation Conference, 2017.

Beygi, M.R. (2016). Development of Compositional Three-phase Relative Permeability and Hysteresis Models and Their Application of EOR Processes, PhD dissertation.

Task 5.0 - Parameter Estimation and Uncertainty Quantification

In order to estimate reservoir properties (both flow and geomechanical) and to assess the uncertainty associated with the estimation of these properties using sparse measurements, it is necessary to develop not just a single model, but a suite of equiprobable models. Thus it is useful to develop a stochastic approach that can provide suitable candidates for the reservoir at low computational costs.

Development of a multiple-realization optimizer coupled with IPARS

This work developed an assisted history matching tool, namely UT-OPT, in order to realize and run IPARS simulations to be in good agreements between observed and simulated pressure anomalies obtained from pulse testing experiments. **Figure 5.1** shows a framework of UT-OPT. UT-OPT consists of three modules: input builder, linker to reservoir simulators, and optimizer. The builder is used to generate ASCII input data files that are imported to one of the optimization algorithms to be executed. The input files are categorized as algorithm parameters (e.g., generation number, population size, and simulator type); uncertain parameters (e.g., permeability); response parameters that are targeted for quality check of reservoir models (e.g., amplitude, frequency, and phase); and watch parameters that are untargeted for quality check (e.g., production rate). In addition to IPARS, commercial simulators are externally linked to UT-OPT. The optimizer contains genetic algorithm (GA) (Goldberg 1989) as a global-objective optimizer and non-dominated sorting genetic algorithm-II (NSGA-II) (Deb et al. 2002) as a multi-objective optimizer. Dynamic goal programming and successive linear-objective-reduction modules are advanced options that can be coupled with NSGA-II to improve the rate of convergence with a small loss in diversity-preservation for solving a many-objective problem in case $M > 4$ (Min et al. 2014, 2015). For reducing the computational cost associated with the generational algorithms, UT-OPT has the capability to run multiple simulations concurrently. Also, each simulation can be executed in high-performance parallel computing environments. This general-purpose tool can be used to perform sensitivity analysis, history matching, production forecasts, economic analysis, and uncertainty analysis. UT-OPT was written in C++ programming language.

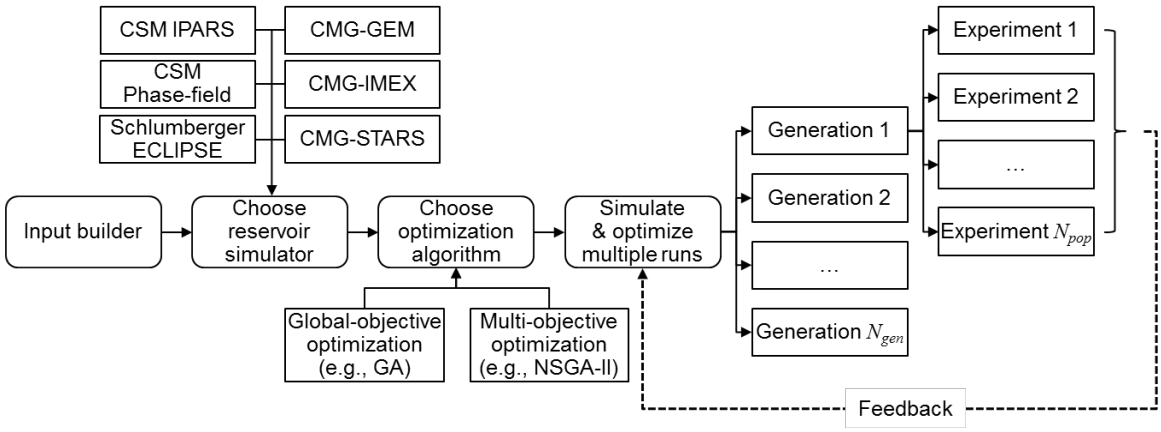

Figure 5.1. The framework of an assisted history matching tool, namely UT-OPT.

Table 5.1 describes a flow chart of the evolutionary process adopted in GA and NSGA-II. This iterative process performs different genetic operations on a pool of solutions. Let P and Q be the parent population and the offspring population, respectively: $\mathbf{p} \in$ P and $\mathbf{q} \in$ Q. The initial parent population P_0 consists of N_{pop} solutions that are generated by random or based on prior knowledge. Here, N_{pop} is the population size (i.e., ensemble size) per generation. At each generation, Q is created by recombining the qualified members in the mating pool $R = P \cup Q$ using two genetic operators: crossover **(Table 5.2)** and mutation **(Table 5.3).** Let P_r, P_c, and P_m be the random probability at each genetic operation, the probability of crossover, and the probability of mutation, respectively. The evolutionary process activates crossover if $P_r < P_c$ and then does mutation if $P_r < P_m$. Both P_c and P_m are specified a priori, in general. Because most solutions are created by crossover in genetic algorithm, typical values of P_c and P_m are employed through the paper: P_c is 0.9 and P_m is 0.1. Here, $r_c \in [1, N]$ is the crossover point that switches all genes after that point. $r_m \in [1, N]$ is the mutation point at which the random variable is altered in the range of its lower and upper limits. Note that both r_c and r_m are picked by random at each genetic operation. More details on crossover and mutation can be found in Goldberg (1989). The termination condition of the evolutionary process is the achievement of a pre-specified tolerance level or the maximum number of generations (i.e., iterations). Let the maximum number of generations be N_{gen}, then the maximum number of evaluations $N_{eval} = N_{gen} \times N_{pop}$.

Evolutionary process

1 : **INITIALIZE** the parent population $P_{t=0}$ with N_{pop} solutions generated based on prior knowledge or by random. The initial offspring population $Q_{t=0} = Ø$.
2 : **EVALUATE** each parent solution in P_0.
3 : **while** *termination condition is not achieved* **do**

```
4  :     t = t + 1.
5  :     SELECT N_pop superior solutions from the mating
         pool R_t = P_{t-1} ∪ Q_{t-1}.
6  :     UPDATE the parent population P_t with the selected
         solutions.
7  :     CROSSOVER pairs of the parent solutions for
         creating N_pop-sized Q_t.
8  :     MUTATE the resulting offspring population Q_t.
9  :     EVALUATE each offspring solution in Q_t.
10 :  end
```

Table 5.1—Pseudo code of the evolutionary process used in genetic algorithm (GA) and non-dominated sorting genetic algorithm-II (NSGA-II).

Crossover

```
1  :  i = 1
2  :  while i < N_pop do
3  :     GENERATE the random probability P_r ∈ [0, 1]
4  :     SELECT two parent members p_i and p_{i+1}
5  :     if P_r < P_c then
6  :        GENERATE the crossover point r_c ∈ [1, N]
7  :        q_i   = {p_{i,1}, ..., p_{i,r_c}, p_{i+1,r_c+1}, ..., p_{i+1,N}}
8  :        q_{i+1} = {p_{i+1,1}, ..., p_{i+1,r_c}, p_{i,r_c+1}, ..., p_{i,N}}
9  :     else
10 :        q_i   = p_i
11 :        q_{i+1} = p_{i+1}
12 :     end
13 :     i = i + 2
14 :  end
```

Table 5.2—Pseudo code of crossover used for creating new solutions in the evolutionary process.

Mutation

```
1  :  i = 1
2  :  while i ≤ N_pop do
3  :     GENERATE the random proabability P_r ∈ [0, 1]
4  :     if P_r < P_m then
5  :        GENERATE the mutation point r_m ∈ [1, N]
6  :        GENERATE the random variable
            q*_{i,r_m} ∈ [q^min_{r_m}, q^max_{r_m}] at the mutation point r_m
7  :        q_i = {q_{i,1}, ..., q_{i,r_m-1}, q*_{i,r_m}, q_{i,r_m+1}, ..., q_{i,N}}
8  :     end
```

```
9  :      i = i + 1
10 :  end
```

Table 5.3—Pseudo code of mutation used for creating new solutions in the evolutionary process.

The selection process is the main difference between GA and NSGA-II. GA is a point search tool that explores the single global-optimum having the smallest objective-sum. Conventionally, N_{pop} solutions are selected from the mating pool R in the ascending order of their objective-sum values. On the other hand, NSGA-II is designed to provide trade-off solutions that are not only converged on the POF but also uniformly distributed along the POF. The trade-off relationship is achieved by non-dominated sorting **(Table 5.4)** and crowding-distance sorting **(Table 5.5).** In NSGA-II, any solution **x** in the mating pool R has two attributes: non-domination rank ($\mathbf{x}_{\text{rank}}$) and crowding distance ($\mathbf{x}_{distance}$). Deb et al. (2002) denote the crowded-comparison operator ($<_n$) that guides the multi-dimensional selection process of NSGA-II toward a uniformly spread-out POF as:

$$\mathbf{x}^1 <_n \mathbf{x}^2 \text{ if } \{\mathbf{x}^1_{\text{rank}} < \mathbf{x}^2_{\text{rank}}\} \text{ or } \{(\mathbf{x}^1_{\text{rank}} = \mathbf{x}^2_{\text{rank}}) \text{ and } (\mathbf{x}^1_{distance} > \mathbf{x}^2_{distance})\}, \quad (1)$$

where $\mathbf{x}^1 \in$ R and $\mathbf{x}^2 \in$ R. That is, NSGA-II primarily prefers solutions with lower (superior) non-domination ranks. If solutions have the same rank, solutions in a lesser crowded region are preferred.

Let F_i be the ith non-dominated front composed of solutions having $\mathbf{x}^i_{\text{rank}}$. In NSGA-II, selecting N_{pop} qualified solutions from the mating pool R requires finding F_n where the cumulative number of solutions from F_1 to F_n exceeds N_{pop}. F_n is the only front in which crowding-distance sorting is activated to select $N^*_{F_n}$ out of $|F_n|$ solutions by pruning solutions located in a denser crowded region of that front as:

$$N^*_{F_n} = N_{pop} - \sum_{i=1}^{n-1} |F_i|. \quad (2)$$

In Table 5.5, $F_n[i]_m$ refers to the mth objective function value of the ith solution in the front F_n. $f_m^{\min}$ and $f_m^{\max}$ are the minimum and maximum values of the mth objective function in the same front. More details on NSGA-II can be found in Deb et al. (2002).

Non-dominated sorting

```
1  :  for each a ∈ R
2  :     S_a = Ø
3  :     n_a = 0
4  :     for each b ∈ R
5  :        if (a ≺ b) then
6  :           S_a = S_a ∪ {b}
7  :        else if (b ≺ a) then
8  :           n_a = n_a + 1
```

```
        end
    end
    if n_a = 0 then
        a_rank = 1
        F_1 = F_1 ∪ {a}
    end
    i = 1
    while F_i ≠ Ø do
        B = Ø
        for each a ∈ F_i
            for each b ∈ S_a
                n_b = n_b − 1
                if n_b = 0 then
                    b_rank = i + 1
                    B = B ∪ {b}
                end
            end
        end
        i = i + 1
        F_i = B
    end
end
```

Table 5.4—Pseudo code of non-dominated sorting in NSGA-II.

Crowding-distance sorting

```
l = |F_n|
while i ≤ l do
    set F_n[i]_distance = 0
end
while m ≤ M do
    F_n = sort(F_n, m)
    F_n[1]_distance = F_n[l]_distance = ∞
    i = 2
    while i ≤ l − 1 do
        F_n[i]_distance = F_n[i]_distance
                        + (F_n[i + 1]_m − F_n[i − 1]_m)/(f_m^max − f_m^min)
        i = i + 1
    end
end
```

Table 5.5—Pseudo code of crowding-distance sorting in NSGA-II.

Table 5.6 compares computational complexity of sorting algorithms in GA and NSGA-II in case all solutions exist in the same non-dominated front. The multi-dimensional search toward the POF requires greater time overhead than the point search due to the number of objectives. Nonetheless, the larger complexity would be affordable where most of the execution time in solving real-world problems is taken in the fitness evaluation of the evolutionary process (Davis 1991). Note that the efficacy of POF search also depends on the number of objectives. Solving a high-dimensional objective problem needs to couple preference-ordering or objective-reduction schemes with the evolutionary process (Saxena et al. 2013;

Min et al. 2014, 2015; Deb and Jain 2015; Jain and Deb 2015), but it is out of scope for this work. We clarify that the number of objectives in this study is restricted to two.

Sorting Algorithm	Complexity
Descending fitness values (Goldberg 1989)	$O(N_{pop}^2)$
Non-dominated sorting (Deb et al. 2002)	$O(MN_{pop}^2)$
Crowding-distance sorting (Deb et al. 2002)	$O(MN_{pop}\log N_{pop})$

Table 5.6—Computational complexity of sorting algorithms in one generation of the evolutionary process. The total complexity is the computational complexity multiplied by the number of generations.

Optimal design of hydraulic fracturing in porous media using the phase field fracture model coupled with genetic algorithm

We present a framework for the coupling of fluid-filled fracture propagation and a genetic inverse algorithm for optimizing hydraulic fracturing scenarios in porous media. Fracture propagations are described by employing a phase field approach, which treats fracture surfaces as diffusive zones rather than of interfaces. For detailed explanations in phase field, please refer to Lee et al. (2016). Performance of the coupled approach is provided with applications to numerical experiments related to maximizing production or reservoir history matching for emphasizing the capability of the framework. In this section, we demonstrate the minimization problem, which was history matching of fractured volume. We clarify that the domain size of the example herein is designed as lab-scale for saving computational costs accompanied with multiple phase field runs during optimization. The example runs 20 experiments concurrently in each generation, and every phase field fracture simulation is executed with 4 parallel processors.

This example solves a minimization problem to explore the global minimum having the smallest discrepancy between actual (reference) and simulated area of fractures. The actual areas of fractures were computed using the simulation results of the reference field model shown in Figure 5.2. Three parallel fractures are positioned in the computational domain $\Omega = (0\text{ m}; 4\text{ m})^2$.

The critical energy release rate is chosen as $G_c = 1\ \text{Nm}^{-1}$, Young's modulus is $E = 10^8$ Pa, and Poisson ratio is set to $\nu = 0.2$. The relationship to the Lame coefficients μ and λ is given by:

$$\mu = \frac{E}{2(1+\nu)}, \qquad \lambda = \frac{\nu E}{(1+\nu)(1-2\nu)}. \tag{3}$$

For the fluid parameters, Biot's coefficient is set as $\alpha = 1$, $M = 10^8$ Pa, $\eta_R = \eta_F = 10^3\ \text{Ns/m}^2$, the reservoir permeability is $K_R = 1\text{D}$, $q_F = 60$, $c_F = 10_{-12}\ \text{Pa}^{-1}$, and the density $\rho = 1{,}000\ \text{kg/m}^3$.

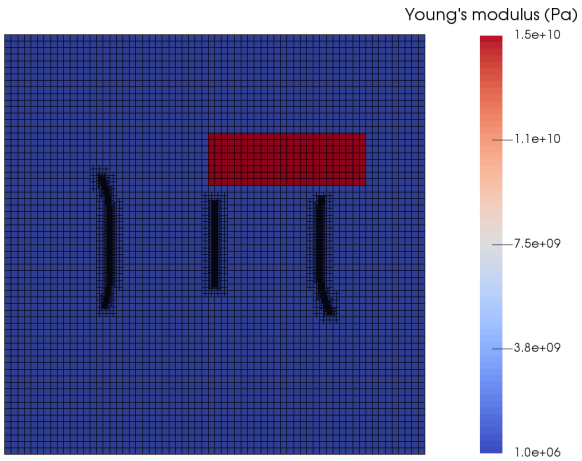

Figure 5.2. Propagated fractures at time step n = 250 with heterogeneous E values of the reference model.

The variable vector **x** of this minimization problem in Equation (31) is set as:

$$\mathbb{x} = \{x_{1,b}, x_{2,b}, y_{1,b}, y_{2,b}, E_{in}, E_{out}\}, \tag{4}$$

where $x_{1,b}$ is x-coordinate of the bottom-left corner of the bar, $x_{2,b}$ is x-coordinate of the upper-right corner of the bar, $y_{1,b}$ is y-coordinate of the bottom-left corner of the bar, $y_{2,b}$ is y-coordinate of the upper-right corner of the bar, E_{in} is Young's modulus of inside the bar, and E_{out} is Young's modulus of outside the bar. The bottom-left corner of the domain is taken to be the origin of the domain. The range of each variable is as follows: $x_{1,b}$, x2,b ∈ [0 m; 4 m]; $y_{1,b}$, $y_{2,b}$ ∈ [0 m; 4 m]; E_{in} ∈ [10^6 Pa, 10^{10} Pa]; and E_{out} ∈ [10^7 Pa, 10^9 Pa]. We intentionally made genetic algorithm more difficult to converge by giving a wide range for Young's modulus.

The objective function for this example is the absolute average percent error derived as:

$$\arg\min_{\mathbb{x}\in\mathbb{R}^N} f(\mathbb{x}) = \arg\min_{\mathbb{x}\in\mathbb{R}^6} \frac{1}{N_{obs}} \sum_{i=1}^{N_{obs}} \left| \frac{V_{f,i}^{ref} - V_{f,i}}{V_{f,i}^{ref}} \right| \times 100(\%), \tag{5}$$

where V_f^{ref} is the fracture area of the reference solution and N_{obs} is the number of observations. In this example, N_{obs} = 1 as V_f^{ref} measured at the last time step is the only observation data used to calculate the objective function.

Operating parameters of hydraulic fracturing are fixed in all phase-field runs: the number of fractures is three, injection rate is constant at each fracture interval, and fracture spacing between the inner fracture and each outer fracture is constant 1 m. At the last time step n = 250, the reference model yields the total

area of fractures $V_f^{ref} = 0.00974681 m^2$, which results from $x_{1,b} = 0.5$ m, $x_{2,b} = 2.0$ m, $y_{1,b} = 2.5$ m, $y_{2,b} = 3.0$ m, $E_{in} = 10^{10}$ Pa, and $E_{out} = 10^8$ Pa.

Figure 5.3 illustrates the numerical results for selected generations and experiments. Each generation had 20 experiments and 10 generations were tested. Since no conditions between E_{in} and E_{out} were provided, we observed some cases with $E_{in} < E_{out}$ that yielded unfavorable simulation results during earlier generations. After the fourth generation, it seems that most experiments get closer to the reference solution in terms of the position of the bar.

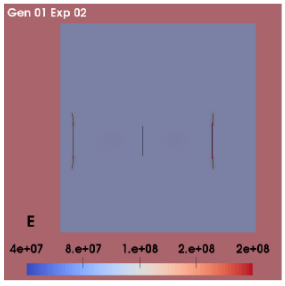

(a) Gen. 1 Exp. 02

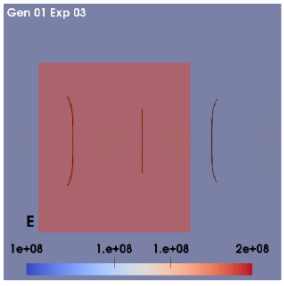

(b) Gen. 1 Exp. 02

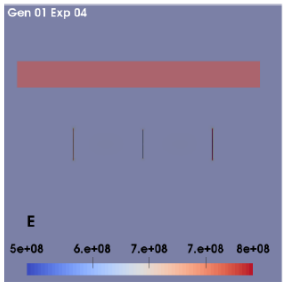

(c) Gen. 1 Exp. 04

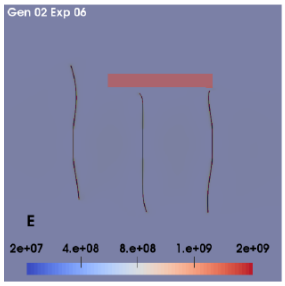

(d) Gen. 2 Exp. 06

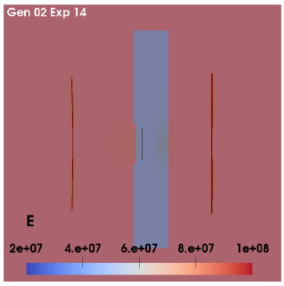

(e) Gen. 2 Exp. 14

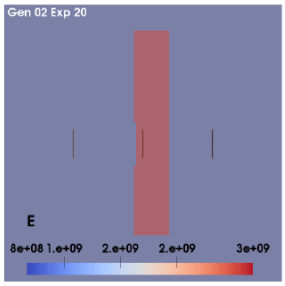

(f) Gen. 2 Exp. 20

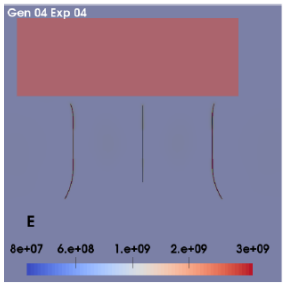

(g) Gen. 4 Exp. 04

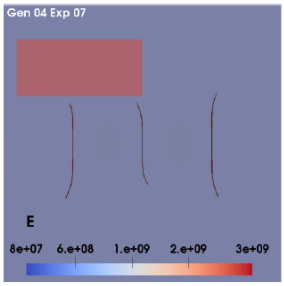

(h) Gen. 4 Exp. 07

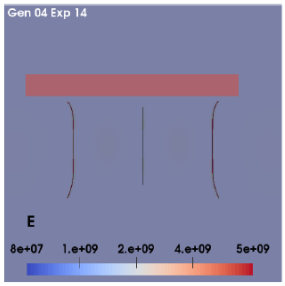

(i) Gen. 4 Exp. 14

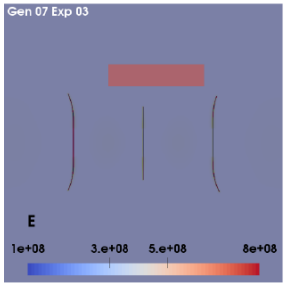

(j) Gen. 7 Exp. 03

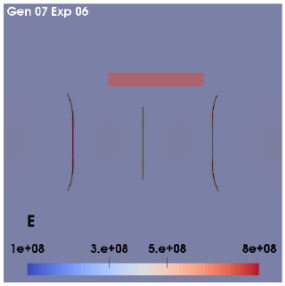

(k) Gen. 7 Exp. 06

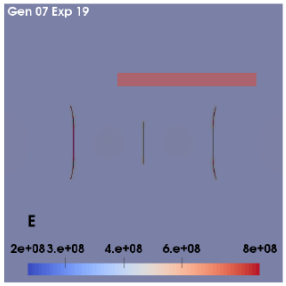

(l) Gen. 7 Exp. 19

Figure 5.3. Illustrates the numerical results for selected generations (Gen = 1, 2, 4, and 7) and experiments (Exp.). Each row indicates different generations. We observe a convergence of the solution to the reference model.

Consequently, Figure 5.4(a) provides the optimized solution similar to the reference solution shown in Figure 5.2. Interestingly, the thickness of the block was a less crucial factor to the performance of genetic algorithm because the phase field model did not allow fractures to penetrate the bar. Figure 5.4(b) shows the stable decrease in the objective function values from the first to the seventh generations. As most experiments were assimilated in the seventh generation, the results from the eighth to the tenth generations are omitted in this figure. Notwithstanding the small positive absolute average percent error, it seems that all solutions arrive near the global minimum (i.e., reference model) in the seventh generation. Employing faster inverse algorithms [8] or coupling a surrogate model with the forward model [50] would contribute to saving computational costs for solving more high-dimensional complex problems. It is also anticipated that reflecting reservoir uncertainty on the parameters adjusted in these examples would deliver more realistic outcomes in future works.

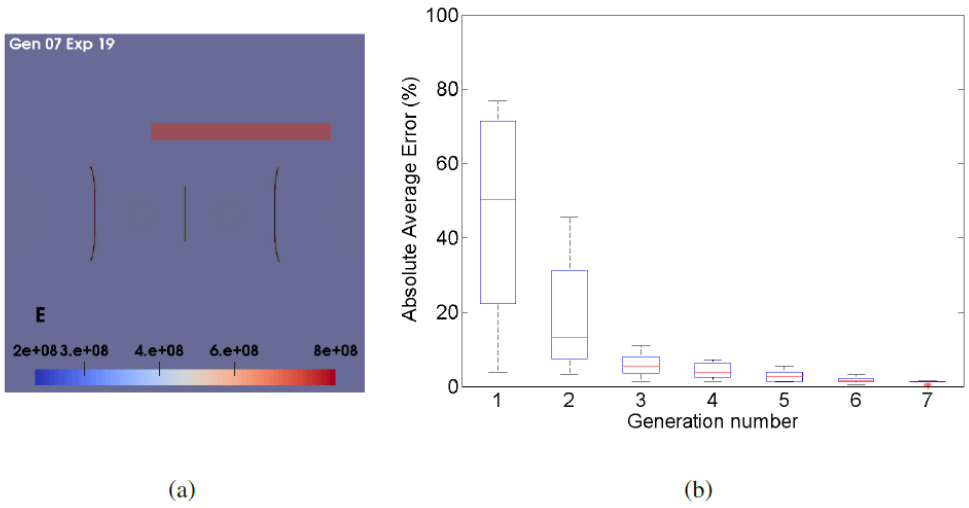

Figure 5.4. Evolution of objective function values for the history matching problem: (a) the optimal solution and (b) convergence of objective function values.

References

Bangerth, W., Klie, H., Wheeler, M. F., Stoffa, P. L., and Sen, M. K. On optimization algorithms for the reservoir oil well placement problem. Computational Geosciences, 10(3):303–319, 2006.

Davis, L. 1991. Handbook of Genetic Algorithms, first edition. New York: Van Nostrand Reinhold.

Deb, K., Pratab, A., Agrawal, S. et al. 2002. A Fast Elitist Non-Dominated Sorting Genetic Algorithm for Multi-Objective Optimization: NSGA-II. IEEE T. Evolut. Comput. 6 (2): 182–197.

http://doi.org/10.1109/4235.996017.

Deb, K. and Jain H. 2014. An Evolutionary Many-Objective Optimization Algorithm Using Reference-Point-Based Nondominated Sorting Approach. Part I: Solving Problems with Box Constraints. IEEE Trans. Evol. Comput. 18 (4): 577–601. http://doi.org/10.1109/TEVC.2013.2281535.

Goldberg, D. E. 1989. Genetic Algorithms in Search, Optimization, and Machine Learning, first edition. Reading: Addison-Wesley Professional.

Jain, H. and Deb, K. 2014. An Evolutionary Many-Objective Optimization Algorithm Using Reference-Point-Based Nondominated Sorting Approach. Part II: Handling Constraints and Extending to an Adaptive Approach. IEEE Trans. Evol. Comput. 18 (4): 602–622. http://doi.org/10.1109/TEVC.2013.2281534.

Lee, S., Mikelic, A., Wheeler, M. F., and Wick, T. Phase-field modeling of proppant filled fractures in a poroelastic medium. Computer Methods in Applied Mechanics and Engineering, 312: 509 – 541, 2016. Phase Field Approaches to Fracture.

Min, B., Kang, J. M., Chung, S. et al. 2014. Pareto-Based Multi-Objective History Matching with Respect to Individual Production Performance in a Heterogeneous Reservoir. J. Petrol. Sci. Eng. 122: 551–566. http://doi.org/10.1016/j.petrol.2014.08.023.

Min, B., Park, C., Jang, I. S. et al. 2015. Development of Pareto-Based Evolutionary Model Integrated with Dynamic Goal Programming and Successive Linear Objective Reduction. Appl. Soft Comput. 35: 75–112. http://doi.org/10.1016/j.asoc.2015.06.007.

Min, B., Park, C., Kang, J., Park, H., Jang, I. Optimal well placement based on artificial neural network incorporating the productivity potential. Energy Sources, Part A: Recovery, Utilization, and Environmental Effects, 33(18):1726–1738, 2011.

Saxena, D. K., Duro, J. A., Tiwari, A. et al. 2013. Objective Reduction in Many-Objective Optimization: Linear and Nonlinear Algorithms. IEEE Trans. Evol. Comput. 17 (1): 77–99. http://doi.org/10.1109/TEVC.2012.2185847.

Status of Project Schedule and Major Goals /Milestones of Project

The project schedule/timeline is shown in the following.

Task Name	Assigned Resource	BP 1				BP 2				BP 3			
		Q1	Q2	Q3	Q4	Q1	Q2	Q3	Q4	Q1	Q2	Q3	Q4
Task 1 .0 - Project management, planning & reporting	***Wheeler***	○											○
Milestone A: Update Project Management (10/30/2014)		**A**											
Milestone B: Kick off meeting (11/30/2014)		**B**											
Task 2.0 -Conduct Laboratory Experiments for Petrophysical and Hydro-mechanical Rock Properties	***Espinoza***	○									○		
Subtask 2.1:Develop Plan for Design of Experimental Apparatus and Rock Property Testing													
Milestone C. Plan for the design of the experimental equipment and the tests to be completed				**C**									
Subtask 2.2: Experimental Apparatus Fabrication, Setup and Calibration and Sample Acquisition													
Milestone D. List of representative rock samples acquired for testing completed.					**D**		◆						
Milestone E. Complete triaxial cell setup and initiate testing.							**E**						
Subtask 2.3: Measurement of basic mechanical properties													
Milestone F. Interim report of measurement of basic rock properties									**F**				
Subtask 2.4 Measurement of Advanced Mechanical Properties with CO2-Specific Loadings													
Milestone G. Complete report that summarizes the activities, rock testing, and results in Task 2.0.										**G**			
Task 3.0 -Upscale by Completing Bridge from Laboratory to Field Scales	***Wheeler***			○									○
Subtask 3.1: Computation of effective parameters for flow and mechanics													
Milestone H. Document homogenization and mortar method for flow and mechanics equations for sub-inch and larger scales respectively.									**H**				
Subtask 3.2: Computation of effective parameters for coupled thermal-geomechanical processes for CO2 Specific Loadings													
Milestone I. Complete report that summarizes the activities and results in Task 3.0 conducted for upscaling lab measurements including a description of the development of homogenization schemes for naturally fractured and heterogeneous rocks.											**I**		
Task 4.0 - Simulator Development and Modeling CO2 Storage Field Scale Studies	***Delshad***	○											○
Subtask 4.1:Simulator Development with Numerical Schemes for Couples Processes													
Milestone J. Initiate Simulator Development with Numerical Schemes for Coupled Processes					**J**								
Milestone K. Complete report that describes the enhanced IPARS simulator developed in Subtask 4.1, and include the IPARS module for geomechanics.									**K**				
Subtask 4.2: Model CO2 Storage Field Sites and Perform Simulations													
Milestone L. Complete reports containing a description of the first selected field site (Site one), the model(s) developed, and the results of the simulations and history matching performed in Subtask 4.2.										**L**			
Milestone M. Complete report containing a description for the second selected field site (Site two), the model(s) developed, and the results of the simulations and history matching performed in Subtask 4.2.												**M**	
Task 5.0 -Parameter Estimation and Uncertainty Quantification	***Srinivasan***							○					○
Subtask 5.1: Ensemble Filtering approach for multi-parameter estimation													
Milestone N. Initiate parameter estimation and uncertainty quantification									**N**				
Subtask 5.2 : Uncertainty Qualification													
Milestone O. Report containing a description of the Task 5.0 computational studies and analyses completed for (1) using the ensemble filtering approach for multi-parameter estimation; and (2) uncertainty quantification conducted with the adaptive response surface-based methodology.													**O**
Task 6.0 - Integrated Results to Generate Geomchanical Screening Tool/Workflow	***Wheeler***										○		○
Milestone P. Report that includes the geomechanical workflow, provides the accompanying documentation/user's guide, and summarizes the activities and results performed in Task 6.0 for the workflow generation.													**P**

Major goals/milestones

The following table lists status of the project milestones. All planned milestones have been met.

Project Milestones

Budget Period	Task/ Subtask	Milestone ID/Description	Planned Completion	Verification Method*
1	**1.0**	A. Updated Project Management Plan	10/30/2014	Project Management Plan file
1	**1.0**	B. Kickoff Meeting	11/30/2014	Presentation file
1	**2.0/2.1**	**C. Plan for the design of the experimental equipment and the tests to be completed.**	3/30/2015	**Completed**
1	**2.0/2.2**	**D. List of representative rock samples acquired for testing completed.**	6/30/2015	**List (06/30/2015)**
2	**2.0/2.2**	**E. Complete triaxial cell setup and initiate testing.**	12/31/2015	**Email to Federal Project Manager (FPM) describing (01/21/2016)**
2	**2.0/2/3**	**F. Interim report of measurement of basic rock properties**	6/30/2016	**Interim report to FPM (06/07/2016)**
3	2.0	G. Complete report that summarizes the activities, rock testing, and results in Task 2.0.	9/1/2016	Quick-look report (09/15/2016)
2	**3.0**	**H. Document homogenization and multiscale mortar methods investigated in study.**	8/30/2016	**Interim report to FPM documenting use of methods**

3	3.0	I. Complete report that summarizes the activities and results in Task 3.0 conducted for upscaling lab measurements including a description of the development of homogenization schemes for naturally fractured and heterogeneous rocks.	12/31/2016	Quick-look Report (01/13/2017)
1	**4.0/4.1**	**J. Initiate Simulator Development with Numerical Schemes for Coupled Processes**	8/30/2015	**Email to FPM describing initiation (08/30/2015)**
2	4.0/4.1	K. Complete report that describes the enhanced IPARS simulator developed in Subtask 4.1, and include the IPARS module for geomechanics.	6/30/2016	Quick-look Report (06/06/2016)
3	4.0/4.2	L. Complete reports containing a description of the first selected field site (Site one), the model(s) developed, and the results of the simulations and history matching performed in Subtask 4.2.	9/1/2016	Quick-look Report (09/15/2016)
3	4.0/4.2	M. Complete report containing a description for the second selected field site (Site two), the model(s) developed, and the results of the simulations and history matching performed in Subtask 4.2.	3/30/2017	Quick-look Report (03/29/2017)
2	**5.0**	**N. Initiate parameter estimation and uncertainty quantification**	6/30/2016	**Email to FPM describing initiation (06/07/2016)**

3	5.0	O. Report containing a description of the Task 5.0 computational studies and analyses completed for (1) using the ensemble filtering approach for multi-parameter estimation; and (2) uncertainty quantification conducted with the adaptive response surface-based methodology.	6/30/2017	Quick-look Report (06/30/2017)
3	6.0	P. Report that includes the geomechanical workflow, provides the accompanying documentation/user's guide, and summarizes the activities and results performed in Task 6.0 for the workflow generation.	8/31/2017	Quick-look Report

PRODUCTS

Journal publications

- Jung, H., Singh, G., Espinoza D.N. and Wheeler, M.F. Quantification of a maximum injection volume of CO2 without geomechanical perturbations using a compositional fluid flow reservoir simulator. ICES Report 17-15, June 2017, The University of Texas at Austin. (accepted for publication in Advances in Water Resources)
- Singh, G., Amanbek, Y. and Wheeler, M.F. Adaptive numerical homogenization for non-linear multiphase flow and transport. ICES Report 17-13, June 2017, The University of Texas at Austin.
- Amanbek, Y., Singh, G., Wheeler, M.F. and vanDuijn, H. Adaptive numerical homogenization for upscaling single phase flow and transport. ICES Report 17-12, June 2017, The University of Texas at Austin.
- Girault, V., Wheeler, Mary F., Kumar, K. and Singh, G. Mixed formulation of a linearized lubrication fracture model in a poro-elastic medium. Mathematical Models and Methods in Applied Sciences, July 2016.
- Girault, V., Kumar, K. and Wheeler, Mary. F. Convergence of iterative coupling of geomechanics with flow in a fractured poroelastic medium, July 2016, Computational Geosciences.
- Wick, T., Singh, G., Wheeler, M.F. Fluid-Filled Fracture Propagation using a Phase-Field Approach and Coupling to a Reservoir Simulator. SPE Journal, SPE-168597, October 2015.
- De Basabe, J.; Sen, M. and Wheeler, M.F. Elastic Wave Propagation in Fractured Media using the Discontinuous Galerkin Method. (Accepted in Geophysics Journal)
- Nwachukwu, A., Min, B., and Srinivasan. S. 2016. Model Selection for CO2 Sequestration using Surface Deformation and Injection Data (under review).
- Min, B., Nwachukwu, A., Srinivasan, S., Wheeler, M.F. 2016b. Selection of Geologic Models Based on Pareto-Optimality Using Surface Deformation and CO2 Injection Data for the In Salah Gas Sequestration Project (submitted)

Books or other non-periodicals: None

Other publications, conference papers, and presentations

- G. Singh, Y. Amanbek, and M. F. Wheeler, Adaptive Homogenization for Upscaling Heterogeneous Porous Medium, SPE Annual Technical Conference, San Antonio, Texas, October 9-11, 2017.

- Y. Amanbek, G. Singh, and M. F. Wheeler, Modeling ow and transport using Enhanced Velocity Mixed Finite Element Method and Numerical Homogenization, Finite Element Rodeo, University of Houston, Houston, Texas, March 3-4,2017.
- Y. Amanbek, G. Singh, and M. F. Wheeler, Multiscale Mehods for Flow and Transport in Porous Media, SIAM Conference on Computational Science and Engineering (CSE17), Atlanta, Georgia, Feb 26 - Mar 3, 2017.
- Presentation, Solvers for Conservative Flow and Transport Algorithms in Porous Media, International Multi-grid Conference, December 5-9, 2016, Bruchal, Germany
- Presentation, New approach for fracture propagation in porous medium, invited colloquium in the Department of Mathematics at Paris VI, December 12, 2016
- Presentation, Methodologies and robust algorithms for subsurface simulators, invited lecture at the Institute of French Petroleum, December 12, 2016.Min, B., Nwachukwu, A., Srinivasan, S., Wheeler, M.F. 2016b. Selection of Geologic Models Based on Pareto-Optimality Using Surface Deformation and CO2 Injection Data for the In Salah Gas Sequestration Project. Presented at the SPE Annual Technical Conference and Exhibition, Dubai, Arab Emirates, 26–28 September. SPE-181569-MS.
- White, D., Ganis, B., Liu, R., and Wheeler, M.F. A near-wellbore study with a Drucker-Prager plasticity model coupled with a parallel compositional reservoir simulator, SPE Reservoir Simulation Conference, 2017.
- Jung, H., Singh, G., Espinoza D.N., Wheeler, M. An integrated case study of the Frio CO2 sequestration pilot test for safe and effective carbon storage including compositional flow and geomechanics. SPE-182710-MS. SPE Reservoir Simulation Conference, Montgomery, TX, 2017.
- Singh, Gurpreet, Venkataraman, Ashwin, Pencheva, Gergina and, Wheeler, Mary F., “A Fully Implicit Reactive Flow Formulation for Low Salinity Waterflooding Process”, 15th European Conference on the Mathematics of Oil Recovery, 29 August - 1 September 2016, Amsterdam, Netherlands
- Venkataraman, Ashwin, Singh, Gurpreet, and Wheeler, Mary F., “Tangent Plane Criteria for Phase Stability Computation for System with Hydrocarbon and Aqueous Phase Components”, 15th European Conference on the Mathematics of Oil Recovery, 29 August - 1 September 2016, Amsterdam, Netherlands
- Wheeler, Mary F., Singh, Gurpreet and, Amanbek, Yerlan, "Upscaling Reservoir Properties Using Single Well Tracer Tests”, Computational Methods in Water Resources, University of Toronto, Canada, June 21-24, 2016.
- Singh, Gurpreet, Ganis, Benjamin and Wheeler, Mary F., “A Parallel Framework for a Multipoint

Flux Mixed Finite Element Equation of State Compositional Flow Simulator", 15th European Conference on the Mathematics of Oil Recovery, 29 August - 1 September 2016, Amsterdam, Netherlands

- Presentation, Development of Geomechanical Screening Tools to Identify Risk: An Experimental and Modeling Approach for Secure CO_2 Storage. Annual Carbon Storage R&D Review, 18 August 2015.
- Presentation, Methodologies and Robust Algorithms for Subsurface Simulators. IOR Norway, April 26, 2016, Norway.
- Presentation, Methodologies and Robust Algorithms for Subsurface Simulators, Energy Institute Workshop, May 4, 2016 (collaborative project between ExxonMobil and The University of Texas at Austin).
- Plenary Session, Phase-Field Modeling of Proppant Filled Fractures in a Poroelastic Medium, Canadian Applied and Industrial Mathematics Society, June 29, 2016 Annual Meeting, Edmonton, Canada.
- Keynote Presentation, Phase-Field Modeling of Proppant Filled Fractures in a Poroelastic Medium, The 11^{th} AIMS Conference on Dynamical Systems Differential Equations and Application, July 4, 2016.
- Keynote Presentation, Computational Screening Tools for Modeling Energy Problems in Porous Media, ECOMAS Congress, June 2016, Greece.
- Keynote Presentation, Computational Screening Tools for Modeling Energy Problems in Porous Media, Energy Day, The University of Texas at Austin, February, 2016.
- Presentation, A Locally Conservative Enriched Galerkin Approximation and an Efficient Solver for Elliptic and Parabolic Problems, MAFELAP, June 2016, UK.
- Presentation, Implementing Multipoint Flux Mixed Finite Elements on Non-Matching Hexahedral Grids Using the Local Flux Method. InterPore, Cincinnati, 9-12 May 2016.
- Presentation, Diffusive Zone Fracture Modeling For Porous Media Applications, SIAM Conference on Mathematical and Computational Issues in Geosciences. Stanford University, California, July 2015.
- Presentation, Coupled flow and geomechanics for fractured poroelastic reservoirs, SIAM Conference on Mathematical and Computational Issues in Geosciences. Stanford University, California, July 2015.
- Poster on application of multi-objective optimization using injection rate and surface deflection data presented at AGU San Francisco, December 2015.

- Al-Hinai, O.; Srinivasan, S.; Dong, R. and Wheeler, M.F. A New Equi-dimensional Fracture Modeling using Polyhedral Cells for Microseismic Data Sets. (Submitted to Journal of Petroleum Technology)

Websites: None

Inventions, patent applications, and/or licenses: None

Other products

- UTKR3P module for hysteretic relative permeability and capillary pressure and integration with IPARS for field scale predictions.
- MFDFrac module for fractured reservoir flow modeling using mimetic finite difference (MFD) and coupling to EnKf for characterizing fractured reservoir.
- Plasticity module for finite geomechanical deformation integrated in IPARS.
- HOMOGEN module two scale homogenization for upscaling flow and transport and integration with IPARS.
- Adaptive homogenization tool combining two-scale homogenization (HOMOGEN) and EVMFE (Enhanced Velocity Mixed Finite Element) scheme.
- UT-OPT toolkit for uncertainty quantification, parameter estimation and non-linear optimization.
- A framework for geomechanical risk assessment of CO2 sequestration scenarios integrating UT-OPT toolkit with IPARS.

PARTICIPANTS & OTHER COLLABORATING ORGANIZATIONS –

- Individuals that have worked on the project: UT research associate, postdoc, graduate students, and PIs
- Other organizations that have been involved as partners: None

CHANGES/PROBLEMS

- Changes in approach and reasons for change: None
- Actual or anticipated problems or delays and actions or plans to resolve them: None
- Changes that have a significant impact on expenditures: None
- Change of primary performance site location from that originally proposed: None

BUDGETARY INFORMATION

In the final quarter, the project expenditures are within the planned baseline costs for the quarter. The updated baseline has been provided by University of Texas Accounting Department.

BASELINE REPORTING QUARTER	Budget Period 3							
	Q1		Q2		Q3		Q4	
	DATE RANGE:10/01/16-12/31/16		DATE RANGE:01/01/17-03/31/17		DATE RANGE:04/01/17-06/30/17		DATE RANGE:07/01/17-09/30/17	
	Q1	Cumulative Total	Q2	Cumulative Total	Q3	Cumulative Total	Q4	Cumulative Total
BASELINE COST PLAN								
Federal Share	$82,315.83	$788,407.19	$82,315.83	$870,723.02	$82,315.83	$953,038.85	$82,315.83	$1,035,354.68
Non-Federal Share	$20,578.48	$197,106.56	$20,578.48	$217,685.04	$20,578.48	$238,263.52	$20,578.48	$258,842.00
TOTAL PLANNED	$102,894.31	$985,513.75	$102,894.31	$1,088,408.06	$102,894.31	$1,191,302.37	$102,894.31	$1,294,196.68
ACTUAL INCURRED COST								
Federal Share	$69,053.97	$798,855.07	$75,585.73	$874,440.80	$27,934.22	$902,375.02	$132,978.98	$1,035,354.00
Non-Federal Share	$0.00	$173,350.61	$0.00	$173,350.61	$64,702.90	$238,053.51	$20,795.49	$258,849.00
TOTAL INCURRED COSTS	$69,053.97	$972,205.68	$75,585.73	$1,047,791.41	$92,637.12	$1,140,428.53	$153,774.47	$1,294,203.00
VARIANCE								
Federal Share	$363,012.95	$594,021.64	$6,730.10	$600,751.74	$54,381.61	$655,133.35	$709,514.96	$1,364,648.31
Non-Federal Share	-$49,857.17	-$83,309.81	$20,578.48	-$62,731.33	-$44,124.42	$210.01	-$43,914.41	-$43,704.40
TOTAL VARIANCE	$313,155.78	$510,711.83	$27,308.58	$538,020.41	$10,257.19	$548,277.60	$558,534.79	$1,106,812.39